AGU ADVANCING EARTH AND SPACE SCIENCES

Earth and Space Science

RESEARCH ARTICLE
10.1029/2024EA003978

Seasonal Cycle in Sea Level Across the Coastal Zone

Rui M. Ponte[1] and **Michael Schindelegger**[2]

[1]Atmospheric and Environmental Research, Inc, Lexington, MA, USA, [2]Institute of Geodesy and Geoinformation, University of Bonn, Bonn, Germany

Key Points:

- Altimetry and tide gauges disclose the complex spatial structure of the mean sea level seasonal cycle from the coast to adjacent deep waters
- Sum of steric and manometric effects, deduced from observations, explains ~65% of the annual sea level variance in global set of tide gauges
- Satellite gravimetry is useful for examining near-shore manometric seasonality but coarse spatial resolution remains a limiting factor

Supporting Information:

Supporting Information may be found in the online version of this article.

Correspondence to:

M. Schindelegger and R. M. Ponte,
schindelegger@igg.uni-bonn.de;
rpoente@aer.com

Citation:

Ponte, R. M., & Schindelegger, M. (2024). Seasonal cycle in sea level across the coastal zone. *Earth and Space Science*, *11*, e2024EA003978. https://doi.org/10.1029/2024EA003978

Received 13 SEP 2024
Accepted 23 NOV 2024

Author Contributions:

Conceptualization: Rui M. Ponte
Formal analysis: Michael Schindelegger
Funding acquisition: Rui M. Ponte
Investigation: Rui M. Ponte, Michael Schindelegger
Methodology: Rui M. Ponte, Michael Schindelegger
Software: Michael Schindelegger
Validation: Rui M. Ponte, Michael Schindelegger
Visualization: Michael Schindelegger
Writing – original draft: Rui M. Ponte, Michael Schindelegger
Writing – review & editing: Rui M. Ponte, Michael Schindelegger

Abstract Data from tide gauges and satellite altimeters are used to provide an up-to-date assessment of the mean seasonal cycle in sea level (ζ) over most of the global coastal ocean. The tide gauge records, where available, depict a ζ seasonal cycle with complex spatial structure along and across continental boundaries, and an annual oscillation dominating over semiannual variability, except in a few regions (e.g., the northwestern Gulf of Mexico). Comparisons between tide gauge and altimeter data reveal substantial root-mean-square differences and only slight improvements in agreement when using along-track data optimized for coastal applications. Quantification of the uncertainty in the altimeter products, inferred from comparing gridded and along-track estimates, indicate that differences to tide gauges partly reflect short-scale features of the seasonal cycle in proximity to the coasts. We additionally probe the ζ seasonal budget using satellite gravimetry-based manometric estimates and steric terms calculated from the World Ocean Atlas 2023. Focusing on global median values, the sum of the estimated steric and manometric harmonics can explain ~65% (respectively 40%) of the annual (semiannual) variance in the coastal ζ observations. We identify several regions, for example, the Australian seaboard, where the seasonal ζ budget is not closed and illustrate that such analysis is mainly limited by the coarse spatial resolution of present satellite-derived mass change products. For most regions with a sufficiently tight budget closure, we find that although the importance of the manometric term generally increases with decreasing water depth, steric contributions are non-negligible near coastlines, especially at the annual frequency.

1. Introduction

Monitoring and predicting variability in coastal sea level is an important scientific endeavor for dealing with coastal inundation, beach erosion, aquifer saline intrusion, and other issues affecting many coastal communities around the globe (Oppenheimer et al., 2019). Aside from long-term sea level rise associated with climate change, variability across a range of temporal scales can have an impact on the coasts (Pugh & Woodworth, 2014). In this context, the seasonal cycle is a climate signal of major relevance, given its substantial amplitude and potential to modulate effects of shorter timescale variability such as that associated with tides and storm surges (Merrifield et al., 2013).

Physical processes affecting the seasonal cycle in the coastal environment can be challenging to simulate, given the presence of large bottom topography changes, complex coastal geometries, strong and variable boundary currents, and intricate dynamics and forcing factors (e.g., see collection of articles in Ponte et al., 2019). Detailed characterization of the diverse behavior in the coastal zone using available observations can lay the ground for robustly testing and enhancing the ability to model and predict the seasonal cycle at the coast and adjacent shallow regions. Such improvements should translate to enhanced capabilities in simulating other climate timescales as well.

A great deal of what is known about sea level variability at the coast has been derived from the global tide gauge network (Holgate et al., 2013, see Figure 1). Pattullo et al. (1955) provided the first detailed look at the seasonal cycle in sea level ζ using 419 tide gauge records distributed globally but much more densely around European and North American coasts. Their efforts included comparisons with steric height estimates based on in situ data taken as close as possible to the tide gauge sites. Similarity between sea level and steric height in some regions were suggestive of isostasy—i.e., the lack of an important bottom pressure or manometric sea level component (Gregory et al., 2019)—but the relation between the two variables was for the most part indeterminate due to the sparse in situ data coverage.

Tsimplis and Woodworth (1994) revisited the global analysis of Pattullo et al. (1955) using more than 1,000 tide gauges, which allowed them to highlight the spatial complexity of the seasonal cycle along the coasts (Figure 1), while also stressing the poor knowledge of its relation to seasonal variability across shelf, continental slope, and

10.1029/2024EA003978

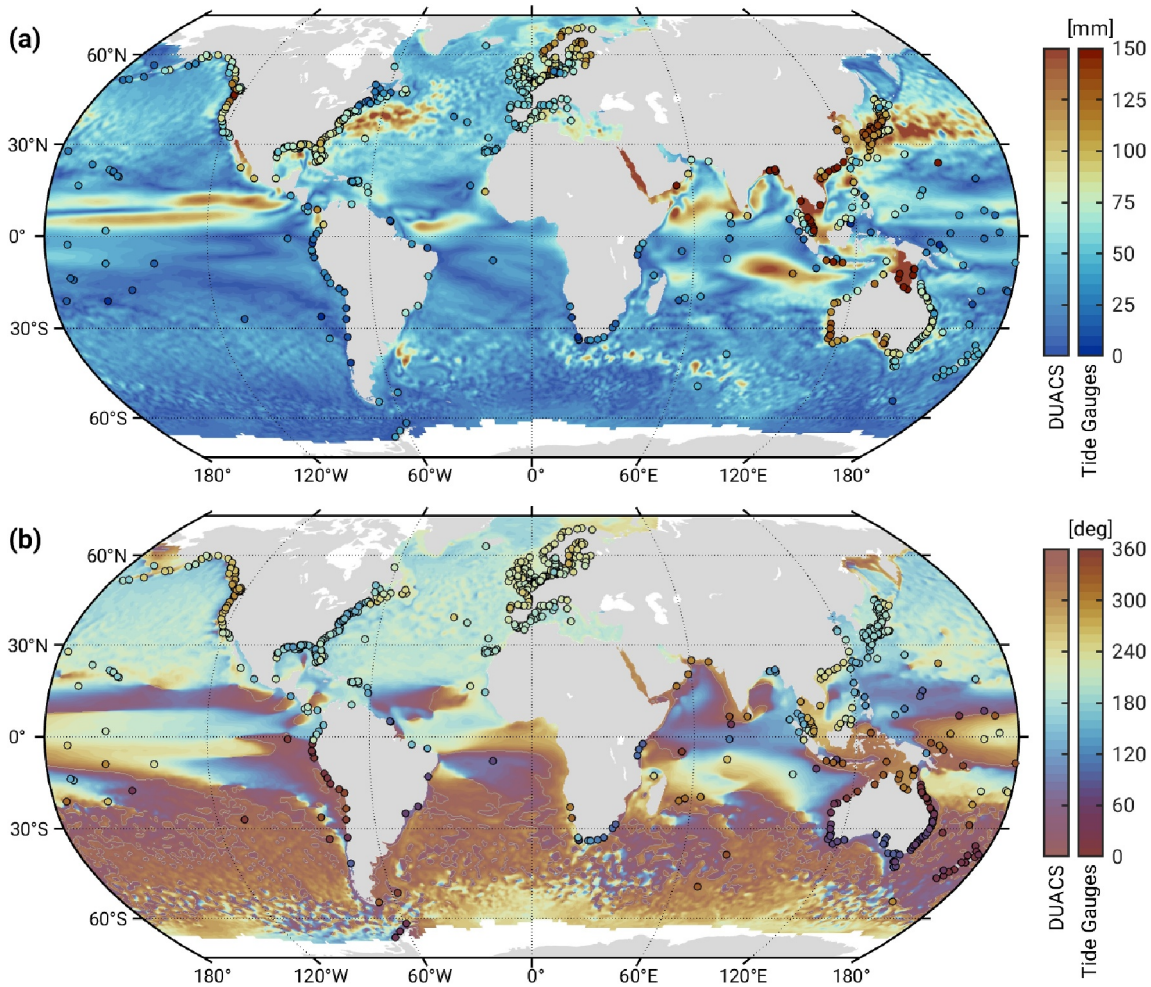

Figure 1. Shown are (a) amplitude (mm) and (b) phase (deg) of the mean annual (Sa) harmonic in sea level calculated for 747 tide gauges (as described in Section 2.1, filled circles) and DUACS gridded altimetry data (Section 2.2). The colormap for altimetry is the same as for tide gauges, except for some additional white opacity. The tide gauge estimates were corrected for the astronomical tide, the pole tide, vertical land motion, and the inverted barometer effect (Section 2.3). Phases are referred to the vernal equinox and therefore lag the common day-of-year phases by ∼80°.

adjacent deep oceans. Tsimplis and Woodworth (1994) pointed to the onset of the satellite altimeter era as an opportunity to establish and understand these relations globally. Comparisons of along-track altimeter data with tide gauges by Vinogradov and Ponte (2010) revealed large differences in the annual cycle in many regions, along with substantial variations in amplitude and phase across the shallow shelves. Similar findings resulted from the global analysis of Ruiz Etcheverry et al. (2015) based on gridded altimeter products. Vinogradov and Ponte (2010) also highlighted the differences in the annual cycle between deep (>200 m) and shallow (<200 m) coastal regions as seen by altimetry observations.

Ray et al. (2021) provided the hitherto most detailed comparison of gridded altimeter fields with tide gauges, also accounting for signals associated with vertical land motion. Root-mean-square (RMS) differences for both annual and semiannual components were around 30% and 40% of the respective RMS signals. Noise in the altimetric retrievals close to the coast may explain some of the reported differences at the tide gauges, and it remains to be seen whether recently available altimeter products using special processing algorithms (e.g., Birol et al., 2017; Birol et al., 2021) can yield closer agreement. A case study for the Baltic Sea-North Sea transition zone based on retracked coastal altimeter data indicated an improved seasonal cycle when compared to tide gauge estimates (Passaro et al., 2015).

Aside from data noise, the differences between tide gauge and altimeter estimates of the seasonal cycle can reflect real short-scale processes that are not adequately sampled by the altimeters right at the coast, and which may be

related to effects of river runoff, wave setup, upwelling, and other boundary circulations (Ray et al., 2021; Ruiz Etcheverry et al., 2015; Vinogradov & Ponte, 2010). More regionally focused studies (e.g., Amiruddin et al., 2015; Bruni et al., 2022; Feng et al., 2015; Gómez-Enri et al., 2012; Volkov & Pujol, 2012) generally support these considerations. The rich dynamics in the coastal zone, as reviewed by Woodworth et al. (2019), imply a complex relation between sea level at the coast and at offshore locations in general (e.g., Hughes et al., 2019). Moreover, simple relations between tide gauge sea level and offshore steric height, of the sort explored initially by Pattullo et al. (1955), are likely to be overwhelmed by the presence of three-dimensional pressure gradients, including those in manometric sea level, across the coastal zone (Bingham & Hughes, 2012).

Our study reexamines the sea level seasonal cycle from the coast to the adjacent deep oceans, as seen by both tide gauges and satellite altimetry. For the latter we consider both along-track and gridded data sets and take advantage of specialized coastal altimetric retrievals by Birol et al. (2017) to reassess the spatial structure of the seasonal cycle very close to the coast. We also leverage available observations of manometric and steric sea level at increasing resolutions (e.g., Cheng & Qi, 2010; Mu et al., 2019; Piecuch et al., 2018) to examine their respective contributions to the sea level seasonal variability and how those vary across the coastal zone. Knowing the spatial structure of the seasonal cycle over the shelf and adjacent deep oceans can lead to better understanding of its manifestation at the coast and of the relevant dynamics and forcing needed to be able to properly simulate and predict it. The detailed description of the seasonal cycle attempted here can provide a solid basis for evaluation of models and the use of altimetry as a space-based tide gauge in the extensive regions where in situ records are totally lacking.

2. Data and Methodology

2.1. Tide Gauges

Our "ground truth" tide gauge data are hourly water level measurements from the GESLA-3 (Global Extreme Sea Level Analysis Version 3) database (Haigh et al., 2022). We initially subset the database to records of at least 9 years of hourly measurements from 1986 onward (cf. Ray et al., 2021) and >75% data completeness within that period. After removing duplicates, short time series in regional clusters, and stations nearly isolated from the open ocean (e.g., in rivers or coastal waterways), we are left with 747 tide gauges. Imposing a looser constraint on full calendar years would permit more stations (Pugh & Woodworth, 2014; Tsimplis & Woodworth, 1994) but also compromise the statistical robustness of the inferred seasonal cycle.

At each station we perform a tidal analysis for 68 constituents using the UTide software package (Codiga, 2011). Apart from a linear trend, and the annual (Sa) and semiannual (Ssa) terms, we also allow for a terannual harmonic in the fit, although not treated in the present study given its small magnitude (median amplitude 7.8 mm). Following Ray et al. (2021), phases are referred to the vernal equinox, and not the beginning of the calendar year as in most previous works. Thus, both Sa and Ssa are written as $A\cos[\Theta(t) - G]$, where A is amplitude, G is phase lag, and the argument $\Theta(t)$ is an integer multiple of the Sun's mean ecliptic longitude, h (Doodson, 1928). The fundamental variable h increases by 360° over one tropical year, such that we have $\Theta(t) = h$ for Sa and $\Theta(t) = 2h$ for Ssa. For the 747 stations analyzed, the median amplitudes are 77.2 mm (Sa) and 22.7 mm (Ssa), with a median standard error of 0.3 mm in both cases. Standard errors of estimated phases grow from 0.3° (median value) at the annual frequency to 0.8° for the semiannual harmonic.

2.2. Altimetry

Along-track sea level anomalies from the X-TRACK project (at Laboratoire d'Etudes en Géophysique et Océanographie Spatiales) form one of three altimetry data sets considered in this work. X-TRACK specifically denotes a post-processing and editing strategy, aimed at maximizing the number of valid near-shore sea surface height retrievals (Birol et al., 2017). In short, the method consists of cleaning both altimeter measurements and corrective terms (e.g., the wet tropospheric delay from the onboard radiometer) for any suspicious data and recomputing the flagged corrections by interpolation or extrapolation of the retained values along the track. Here we use reprocessed 1-Hz sea level anomalies for the Topex/Poseidon, and Jason-1/2/3 missions, available as part of the X-TRACK-L2P product, version 2.1 (simply referred to as X-TRACK hereafter). The data for this product are divided into 27 regions, but four of those (e.g., Hudson Bay, Black Sea) are ignored by us owing to the lack of suitable tide gauges. We analyze time series from March 1993 through to 2017—for consistency with the gridded altimetry described below—and estimate seasonal harmonics, along with a linear trend, at each along-track point featuring at least 75% data completeness. Note that the 1-Hz temporal sampling translates to a ~7-km spacing in

along-track direction. Recent progress in retracking the 20-Hz Jason altimetry waveforms (Birol et al., 2021; Cazenave et al., 2023) has led to a new, higher-resolution altimetry product for coastal applications, but these data are currently provided with seasonal terms removed and are thus not considered here.

We also examine mean seasonal cycle determinations from two gridded, global multi-mission altimetry data sets analyzed over the period 1993–2017. These determinations were provided to us by Richard Ray (NASA Goddard Space Flight Center) and are identical to the estimates deduced and discussed by Ray et al. (2021). The first product subjected to harmonic analysis is the delayed-time (DT) 2018 version of the Data Unification and Altimeter Combination System (DUACS) data (Taburet et al., 2019), disseminated by the Copernicus Marine Service project. The global L4 DUACS grids are discretized at 1/4° in latitude-longitude and were built from measurements of a changing satellite constellation, comprising all available radar altimeters at a given time (ranging from two to six during 1993–2017). In regions ~30 km from the coast, the DUACS DT-2018 sea level anomalies benefit from a median filter in the data selection procedure (Taburet et al., 2019) and a more accurate mean sea surface compared to prior versions (Pujol et al., 2018).

The second gridded set of Sa and Ssa coefficients were fitted to optimally interpolated altimeter time series from the NASA project Making Earth System Data Records for Use in Research Environments (MEaSUREs, Zlotnicki et al., 2019). The MEaSUREs mapping consisted of ordinary kriging on a 1/6° latitude-longitude grid every 5 days, employing sea surface height observations from two simultaneously flying satellites, one from the Topex/Poseidon-Jason reference missions and one polar-orbiting mission (e.g., ERS-1/2, CryoSat-2). Use of less satellites in the MEaSUREs processing likely reduces the product's fidelity in the presence of short spatial-scale structures in the coastal zone. The fundamental corrections applied to both DUACS and MEaSUREs data were very similar to those used for X-TRACK, with a few exceptions regarding, for example, the ocean tide (Ray et al., 2021, Section 2.3).

2.3. Corrections

In comparing tide gauge and altimetric measurements of the seasonal cycle, questions arise as to what adjustments have been, and should be applied to either raw data. Our focus here is on signals in absolute sea level that bear on dynamics. Static effects, which would be relevant to considerations of coastal flooding (Section 1, Sun et al., 2023), are removed from the records. The largest such effect is the ocean's inverted barometer (IB) response to loading by atmospheric pressure (P_a), routinely subtracted from altimetry observations as part of the dynamic atmospheric correction (DAC, Carrère & Lyard, 2003). The three altimeter sources have used various iterations of DAC, in part also changing from mission to mission, yet all based on atmospheric pressures from the European Center for Medium-range Weather Forecasting (ECMWF). One could amend possible differences in the IB correction by restoring the respective DAC fields to each altimetry product, before subtracting a common IB estimate from all data sets (including the tide gauges). However, not all DAC versions are readily available, and supplementary tests have shown that no matter what ECMWF P_a is used to remove the IB signal at tide gauges, our results would barely change. Here we adopt ECMWF ERA-Interim reanalysis data (Dee et al., 2011), as that choice does not favor any particular altimetry product in terms of the DAC (cf. the X-TRACK handbook and Ray et al., 2021). The correction reads $-(P_a - \overline{P_a})/(\rho_0\, g)$, where overbar denotes a spatial average, $g = 9.80665\ \mathrm{m\ s^{-1}}$ is acceleration of gravity, and $\rho_0 = 1029\ \mathrm{kg\ m^{-3}}$ is a mean seawater density. Consistent with the altimetry IB corrections, small variations of ρ_0 with location (~3%) are neglected.

Additional equilibrium effects arise from gravitational tidal forcing and the ocean's response to the annual wobble, that is, the pole tide. All three altimeter sources have adopted the pole tide model of Desai et al. (2015), which suggests annual oscillations in sea level of about 2–3 mm in mid-latitudes, while the Ssa signal is negligibly small (Ray et al., 2021). Next to the annual pole tide, we correct the seasonal harmonics at tide gauges for contributions from the Sa and Ssa astronomical tides, again using gridded estimates provided to us by Richard Ray. The Sa equilibrium tide is very small (1.2 mm at the equator) and most likely still contained in the DUACS and X-TRACK data (but not in MEaSUREs). We thus remove the Sa constituent from the DUACS and X-TRACK harmonics prior to any further analysis.

A final adjustment concerns the seasonal components of crustal displacement, which must be added to the tide gauge estimates of the seasonal cycle in relative sea level (relative to the seafloor) to conform with the absolute sea levels observed by altimetry. To this end, we use satellite gravimetry-based models of annual and semiannual

vertical land motion from Ray et al. (2021). The semiannual deformation rarely exceeds 1 mm (2 mm at station Yakutat, Alaska), while Sa values are larger than 4 mm in a number of regions (Gulf of Alaska, Brazil, Northwest Australia, Gulf of Thailand) and reach 9 mm in the northern Bay of Bengal. The correction accounts for the long wavelengths of crustal loading by geophysical fluids (Ray et al., 2013), which typically explains ∼50% of the annual signal in geodetic station time series (cf. Chanard et al., 2020, and references therein). More localized phenomena, such as anomalous surface runoff (Steckler et al., 2010) or poroelastic deformation (Silverii et al., 2016), can introduce short-scale variability in seasonal vertical land motion, but these effects are limited in magnitude (∼10 mm, Dong et al., 2002) and far from widespread. No effort is made here to account for potential differences in the terrestrial reference frames underlying various satellite orbit solutions and the tide gauge time series. We simply assume that all in situ observations are placed in a center-of-figure frame. The choice also appears to evoke least inconsistency with the DUACS data; see Ray et al. (2021) for a discussion.

2.4. Complementary Data

The provenance of our seasonal cycle estimates in manometric sea level, ζ_m, and steric sea level, ζ_s, is as follows. For ζ_m, we use ∼20 years (April 2002 to December 2021) of nearly continuous, monthly ocean bottom pressure grids derived from space-based gravity field observations collected with the Gravity Recovery and Climate Experiment/-Follow On (GRACE, Tapley et al., 2019) missions. The particular GRACE product examined here is a solution by NASA Goddard Space Flight Center (GSFC, RL06v2.0; Loomis et al., 2019), parameterized in terms of 1° equal-area mass concentration (mascon) blocks and made available on a 1/2° latitude-longitude grid. Mascons are localizing base functions that allow for flexible addition of geophysical constraints to the gravity field estimation, for example, to reduce leakage of mass signals across land-ocean boundaries. Such solutions have previously shown their worth in studies of coastal sea level variability (Mangini et al., 2023; Mu et al., 2019; Piecuch et al., 2018). The GSFC grids can be readily interpreted as estimates of ζ_m in the center-of-figure frame, but they include, through addition of the so-called GAD product (Dobslaw et al., 2017), the effect of spatial mean ocean bottom pressure changes associated with the IB response. Thus, for consistency with the altimetry processing, we subtract at each grid point a time series of the spatial mean atmospheric pressure over the ocean, using the same products and parameters as for the IB correction of the tide gauges (Section 2.3). Prior to harmonic analysis, we further remove jumps and trends associated with major earthquakes, and scale the original equivalent water height values by a factor of 1,000/1,029 (to account for the difference between a representative mean seawater density ρ_0 and the freshwater density assumed in the GRACE solutions; cf. Ponte et al., 2024). As with the IB calculations, effects of small ρ_0 variations with season and location are neglected, as these would change Sa and Ssa ζ_m amplitudes by 1%–3% only in a few locations (Baltic Sea, Gulf of Thailand, river plume areas).

Steric sea levels ζ_s are derived as sum of thermal and haline anomalies in specific volume (cf. Pattullo et al., 1955) from the World Ocean Atlas 2023 (WOA23, Reagan et al., 2024). The WOA23 large database contains objectively analyzed subsurface ocean profiles, collected from, for example, ship-deployed conductivity-temperature-depth packages, bathythermographs, thermosalinographs, gliders, and buoys. Here we use monthly mean climatologies of in situ temperature and practical salinity, formed from observations over 30 years (1991–2020). The analyzed altimetry data thus share 25 years of overlap with WOA23 and ∼19 years with the GRACE records, allowing for adequate comparisons in terms of the mean seasonal ζ, ζ_s, and ζ_m cycles. The WOA23 fields are discretized on the same 1/4° latitude-longitude grid as DUACS and given at 57 standard depth levels from 0 to 1,500 m. In vertically integrating the specific volume quantities, we consider fractional cells computed by us from a modern bathymetry (Schaffer et al., 2016). Although the thermosteric component dominates the annual cycle of ζ_s across most shelf regions, the halosteric Sa amplitude is a significant fraction ($\gtrsim$ 85%) of the total steric Sa amplitude near major river deltas. Salient examples are the deltas of Ganges/Brahmaputra (halosteric Sa amplitude 3–4 cm), Amazonas, Niger, or Irrawaddy (all 2–3 cm in amplitude).

While our emphasis is on inferences from observations, we also consider—for probing the uncertainties of the GRACE and WOA23 seasonal cycles—ζ_m and ζ_s estimates from the Ocean Reanalysis System 5 (ORAS5, Zuo et al., 2017). ORAS5 is a modern, eddy-permitting ocean reanalysis, constructed by sequentially adjusting the forward-integrated state of a general circulation model to agree, within specified uncertainties, with oceanographic observations (e.g., sea surface temperature, Argo floats, altimetric sea level anomalies, but not GRACE). Recent tests made in other contexts (Börger et al., 2023; Gou et al., 2024) lend credence to the ORAS5 bottom pressure and sea level variability across a range of frequencies. We use monthly sea surface height, and three-dimensional temperature and salinity fields, available on the same 1/4° × 1/4° grid as the WOA23 data, and

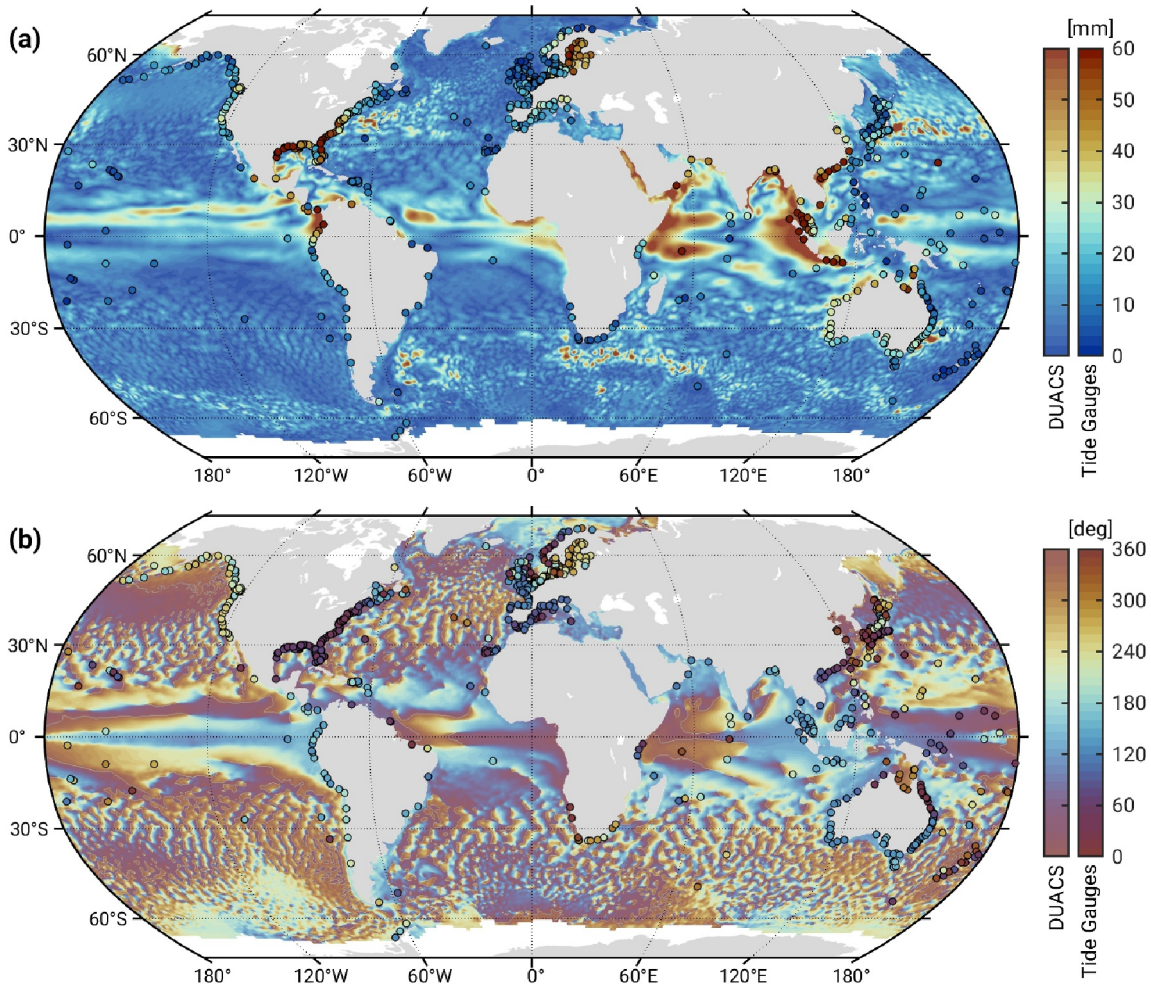

Figure 2. As Figure 1 but for the mean semiannual harmonic (Ssa) in sea level. Corrections for the astronomical tide, vertical land motion, and the inverted barometer effect were applied to the tide gauge estimates (as described in Section 2.3). Phases are referred to the vernal equinox and therefore lag the common day-of-year phases by ∼160°.

deduce ζ_m and ζ_s by solving the proper vertical integrals (see Gou et al., 2024, for details in relation to ζ_m). The analysis period is January 2002 to December 2021, slightly longer than for the GRACE solutions.

3. Results

3.1. Seasonal Cycle at the Coast From Tide Gauges

Amplitudes and phases of the Sa and Ssa harmonics for the tide gauge set analyzed here (Figures 1 and 2) essentially reproduce the major large-scale characteristics of the seasonal cycle discussed by Pattullo et al. (1955), Tsimplis and Woodworth (1994), and Pugh and Woodworth (2014), although based on the non-overlapping altimeter period of analysis (1993–2017). Largest Sa amplitudes (>15 cm) occur in Southeast Asia (northern Bay of Bengal, Gulf of Thailand, South China Sea) and the Gulf of Carpentaria, with generally weakest amplitudes (<10 cm) found at mid-ocean islands. The exceptions are Minamitori Island (24°N, 154°E), which is conditioned by unusually strong wave setup effects (Ray et al., 2021), and Cocos Island (12°S, 97°E), located in a region with large-scale Sa maximum as seen in altimeter observations (Figure 1a).

At the large scale, the annual cycle is characterized by somewhat higher amplitudes at European/North American coasts versus African/South American coasts, a similar contrast between western and eastern Australian coasts, increasing strength of Sa with latitude for the European coast, and decreasing amplitudes the higher the latitude along the eastern North American coast. Superimposed on these broad patterns are finer-scale differences (e.g.,

northwestern US, east and west coasts of Japan and Malaysia) that hint at the presence of relatively local effects. Phases for Sa indicate maxima occurring mostly in the fall season of each hemisphere, but there are differences by as much as a couple of months as one moves along many of the continental coasts. Large phase differences can be seen across narrow stretches of land (e.g., east and west coasts of Malaysia) and there is substantial scatter for mid-ocean islands as well.

Analyses of Ssa (Figure 2) reveal amplitudes mostly <6 cm, with largest values seen for the coasts of Southeast Asia, Indonesia, Colombia, Panama, Gulf of Mexico, and Southeast US. Some of these coasts also exhibit large Sa amplitudes, which as noted by Tsimplis and Woodworth (1994) may indicate the presence of a strong harmonic of the annual cycle, generated through nonlinear dynamics, rather than an intrinsic semiannual cycle. Such is not the case everywhere, though. For example, near-equatorial tide gauges in Sumatra, Ecuador, and Peru, and also in the Gulf of Mexico, actually have Ssa amplitudes larger than those for Sa, and comparable values are also seen in the Southeast US and the Baltic. Mid-ocean islands have Ssa amplitudes mostly <3 cm, bar Minamitori and Pointe La Rue (Mahé Island, Seychelles). The former may again manifest a harmonic of the very strong annual oscillation, whereas Pointe La Rue is located in a broad region with an enhanced semiannual cycle (Figure 2a) associated with a resonance of the equatorial Indian Ocean (Fu, 2007).

Phases for the Ssa term (Figure 2b) are remarkably homogeneous over long stretches of South American, Northeast American, Southeast Asian, Indonesian and Australian coasts. More scatter is found for mid-ocean islands, as with Sa, and also for Japanese and northern European coasts. Here, large phase differences among neighboring sites (e.g., in the southern North Sea, Ireland, and throughout the Japan/East Sea) generally coincide with places of weak Ssa amplitudes (<1 cm). Formal standard errors for phases at the respective tide gauges are not particularly inflated (mostly <3°), suggesting that short-scale phase variability is a genuine feature of the semiannual cycle in these marginal seas. Widening the focus once again, we also find relatively large contrasts in Ssa phases between northern and southern Australia, western and eastern North America, and the Baltic and western Europe (Figures 2b and Tsimplis & Woodworth, 1994).

3.2. Comparison of Tide Gauges and Altimetry

Can the relatively complex behavior of the seasonal cycle at the coast, clear in the tide gauge record, be represented by the altimeter observations? With the typical coarse altimeter sampling, capturing short scales both along and across the coastal zone can be challenging. Before we explore in detail the spatial structure of the seasonal cycle, we revisit the analysis of Vinogradov and Ponte (2010), Ruiz Etcheverry et al. (2015) and Ray et al. (2021) to assess the performance of coastal dedicated altimeter estimates from X-TRACK compared to the gridded DUACS and MEaSUREs products described in Section 2.2. Following Vinogradov and Ponte (2010), we examine comparisons for "shallow" and "deep" estimates, corresponding to average altimeter seasonal cycles calculated for depths shallower and deeper than 200 m. In addition, a "coastal" estimate restricted to "shallow" altimeter data within just 20 km of the tide gauge is also analyzed. In all cases, altimeter values used are limited to a circle of radius 134 km centered on the tide gauge, as in Vinogradov and Ponte (2010).

From the RMS differences and median absolute value differences (MAD) summarized in Table 1, the coastal altimeter estimates account for a substantial portion of the variability seen at the tide gauges. The RMS differences, particularly for shallow and deep estimates, are comparable to those of Ray et al. (2021) for both Sa and Ssa and also those of Ruiz Etcheverry et al. (2015) for Sa (cf. their Table 1), although these studies use somewhat different data and methodology. In comparing residual amplitudes for the different altimeter products, Sa and Ssa statistics for MEaSUREs fare worse than those for DUACS for all groups, and substantially so for coastal estimates (see also Ray et al., 2021). Differences between X-TRACK and DUACS are more subtle. For Sa, X-TRACK yields smaller RMS differences for the shallow and coastal estimates and smaller MAD only for shallow estimates. The RMS differences for Ssa are virtually indistinguishable between X-TRACK and DUACS, although X-TRACK is slightly better when MAD statistics are considered.

A more fine-grained analysis in Figure 3, in terms of gradually decreasing averaging radii for shallow estimates, confirms the tendency for smaller RMS differences with X-TRACK than with DUACS and also a sensitivity to local anomalies in the seasonal cycle. Presence of such "outliers" is implied by the different results when considering RMS and MAD statistics, particularly at distances of <30 km from the tide gauges. The sensitivity is most pronounced for Sa, where a few tide gauges in regions with sharp amplitude and phase transitions (notably Booby Island and Goods Island in the Torres Strait) are much less well represented in the DUACS fields than with

Table 1
RMS Differences (cm) and MAD (cm, in Parentheses) Between Tide Gauge and Altimeter Sa and Ssa[a,b]

	Signal[c]	X-TRACK	DUACS	MEaSUREs
Annual harmonic				
Deep	5.48	2.55 (2.26)	2.48 (2.15)	2.71 (2.50)
Shallow	6.31	1.68 (1.48)	1.74 (1.54)	2.20 (2.17)
Coastal, ≤20 km	6.91	0.80 (0.93)	1.03 (0.90)	1.96 (2.10)
Semiannual harmonic				
Deep	1.78	1.12 (0.98)	1.12 (0.99)	1.18 (1.08)
Shallow	2.15	0.95 (0.80)	0.96 (0.84)	1.14 (1.06)
Coastal, ≤20 km	1.93	0.57 (0.53)	0.57 (0.57)	0.97 (0.88)

[a]Writing Sa or Ssa as $\hat{\zeta}$ in complex notation, the mean RMS difference over n tide gauge (subscript T) and satellite altimetry (S) pairs is $\left[\sum_{i=1}^{n}|\hat{\zeta}_{i,T}-\hat{\zeta}_{i,S}|^2/(2n)\right]^{1/2}$, where n takes values of 391, 570, and 64 for deep, shallow, and coastal areas. These numbers depend on the track geometry in proximity to the tide gauges, the chosen averaging radius, and the width of the continental shelf; cf. Vinogradov and Ponte (2010). Since several densely sampled regions (e.g., Europe) have wide shelves, n is greater for shallow estimates than for deep estimates. [b]MAD values are given by median$\left(|\hat{\zeta}_{i,T}-\hat{\zeta}_{i,S}|_{i=1\ldots n}\right)$. [c]Signal at tide gauges (cm) defined as $\left[\sum_{i=1}^{n}|\hat{\zeta}_{i,T}|^2/2\right]^{1/2}$.

the 7-km along-track values from X-TRACK. Naturally, statistics become less robust when considering smaller radii, owing to the decrease in number of tide gauges included in the analysis. However, averaging over radii >30 km generally yields improved statistics for X-TRACK in both Sa and Ssa cases.

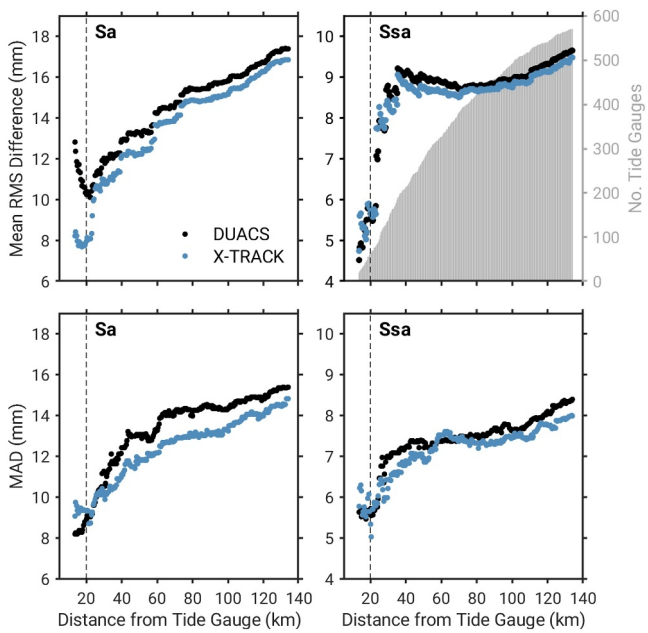

Figure 3. Mean RMS differences and MAD (both in mm) between tide gauge and altimetric (DUACS, X-TRACK) seasonal harmonics for various averaging radii, increasing in 0.5-km steps from 13.5 km (20 tide gauges) to 134 km (570 tide gauges). Only points in water shallower than 200 m are considered for the altimetry averages, such that statistics at 134 km conform with the "shallow" entries in Table 1. The 20-km limit is marked as dashed vertical line, while the number of tide gauges across the different radii is shown in the top right panel.

Focusing on X-TRACK coastal estimates in Table 1, RMS differences amount to ∼12% and 30% of the signal for Sa and Ssa, respectively, underlining the ability of the altimeter data to capture a significant percentage of the seasonal variability seen at the tide gauge locations. Those percentages progressively decrease when considering shallow (27% and 44%) and deep (47% and 63%) estimates. Such dependence of the statistics on the distance from the tide gauge locations indicates considerable spatial variability of the seasonal cycle in the coastal zone. Results in Figure 3 confirm the tendency for larger residuals as data from more distant tide gauges are included.

While slight improvements in the agreement with tide gauges are realized by the use of the X-TRACK product—which is geared toward optimal near-coastal altimetry estimates—it is clear that the differences highlighted in Table 1 and Figure 3 also result from relatively short spatial scale structures that shape the seasonal variability across the coastal zone. We turn next to regional analyses of the tide gauge and altimeter fields to further explore the nature of their differences.

3.3. Seasonal Cycle in the Coastal Zone

Regional detail of the global mean RMS statistics in Table 1, provided in Figure 4, reveals several areas characterized by substantial differences between tide gauge and altimetry. For example, median RMS differences amount to ∼20% of the tide gauge RMS signals for all North American coastal regions and the Baltic Sea in Figure 4, for both Sa and Ssa, and additionally for the Northwest European Shelf, Mediterranean Sea, East China Sea and Bay of Bengal/Gulf of Thailand regions for Ssa. Similar results hold for the Andean region but only two tide gauges are used in those statistics. Some of the regions in Figure 4 provide the focus of the analysis of the spatial structure of the seasonal cycle across the coastal zone discussed in this section. The approach is to show both the gridded DUACS and the along-

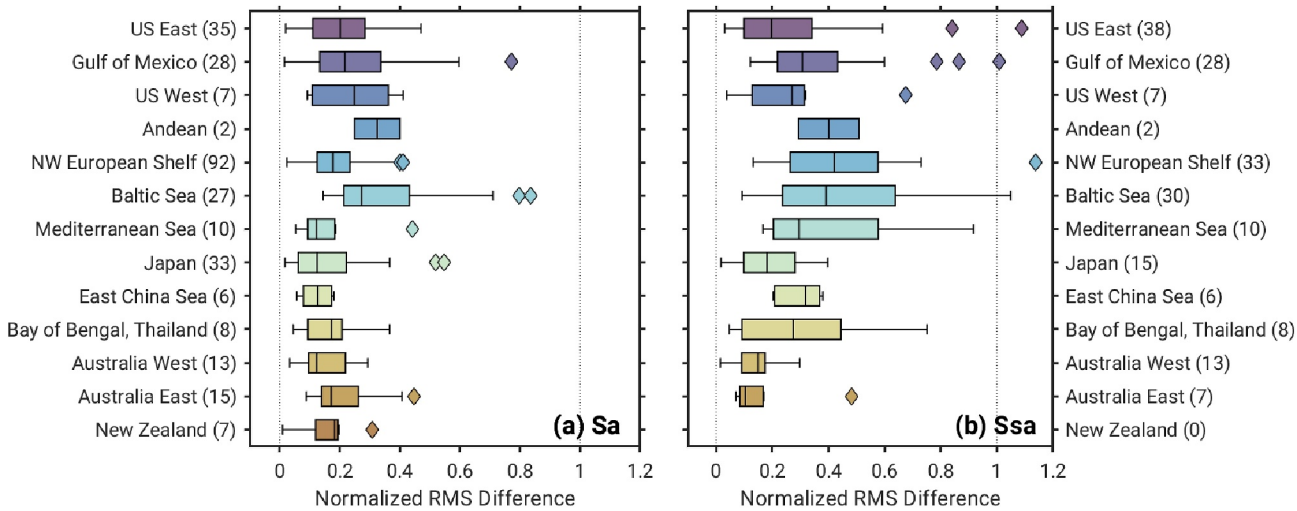

Figure 4. Boxplot of normalized (a) Sa and (b) Ssa RMS differences between tide gauge and coastal altimetry from X-TRACK in 13 regions, as delimited in Figure S1 (Supporting Information S1). The normalization is relative to the signal for each tide gauge, defined as in Table 1. Numbers in parentheses on the two vertical axes show the total count of tide gauges per region, obtained after omitting sites with Sa and Ssa signals smaller than 2.5 and 1.0 cm, respectively. An averaging radius of 70 km was adopted for X-TRACK; the chosen value is a trade-off that allows forming tide gauge-altimetry pairs for Sa in all regions, while emphasizing near-shore signals in the altimetry as much as possible.

track X-TRACK fields together with the tide gauges and highlight the spatial complexity typical of the coastal environment as resolved by the observations. Our focus is on the largest Sa harmonic, but Ssa is also discussed for one representative region with relatively high amplitudes and variable behavior. Not all regions can be discussed in detail, but extra panels for a few coasts are given in Figures S2–S9 in Supporting Information S1, in providing broader context for the analyses in the main text, and also for readers interested in pursuing comparisons with previous regional studies.

The Sa component exhibits a rich variety of behaviors along the North American coasts. We choose to higlight the eastern coast in Figure 5; the western coast has been discussed in detail elsewhere (Ray et al., 2021; Ruiz Etcheverry et al., 2015; Vinogradov & Ponte, 2010), and our findings (see Figure S2 in Supporting Information S1) confirm the large tide gauge and altimeter differences reflective of sharp near-shore gradients in Sa amplitudes. While the amplitudes in Figure 5 tend to decrease with latitude along the coast, from Florida to the Gulf of Maine, the opposite is true offshore. Thus, amplitudes generally increase (decrease) toward the coast south (north) of Cape Hatteras. The continental slope appears to delimit the areas of largest amplitude offshore north of Hatteras, and the largest amplitudes near east Florida and Georgia are confined within the 200-m isobath. Comparing the altimeter and tide gauge amplitudes, we find a somewhat suppressed Sa variability in the western Gulf of Maine tide gauges (Boston, Fort Point, and Portland), whereas coastal enhancement seems to be the case for some Florida tide gauges. As regards phase estimates, they match well south of Hatteras, but there are clear differences for the Mid-Atlantic Bight and again also for the westernmost gauges in the Gulf of Maine.

A striking example of complex spatial behavior is offered by the Sa variability around Japan and the Japan/East Sea (Figure 6, see also Feng et al., 2015). While the eastern coast of the main Japanese islands displays substantial changes in Sa amplitude, both along and across the shelf, the amplitudes on the western coast are more homogeneous. The latter tend to match the amplitudes seen offshore south and east of Japan, hinting at a possible influence from the circulation over the deep oceans. In contrast, the eastern coast of Japan seems much more shielded from the influence of the pronounced annual cycle offshore, particularly where the Kuroshio is well separated from the coast. The altimetric Sa solutions indicate relatively small scale features that do not map onto nearby coastal records (e.g., peak amplitudes of >15 cm on the east side of the Tsugaru Strait, between Honshu and Hokkaido, and a patch of minimum amplitudes south of Tokyo). The tide gauges in the area between Honshu, Shikoku, and Kyushu islands also show somewhat larger amplitudes than the nearby altimetry, perhaps not surprisingly given the constricted geography of the region and the relatively coarse altimeter resolution—there are actually no X-TRACK data available. Phases show much less spatial variability than amplitudes and are characterized by close

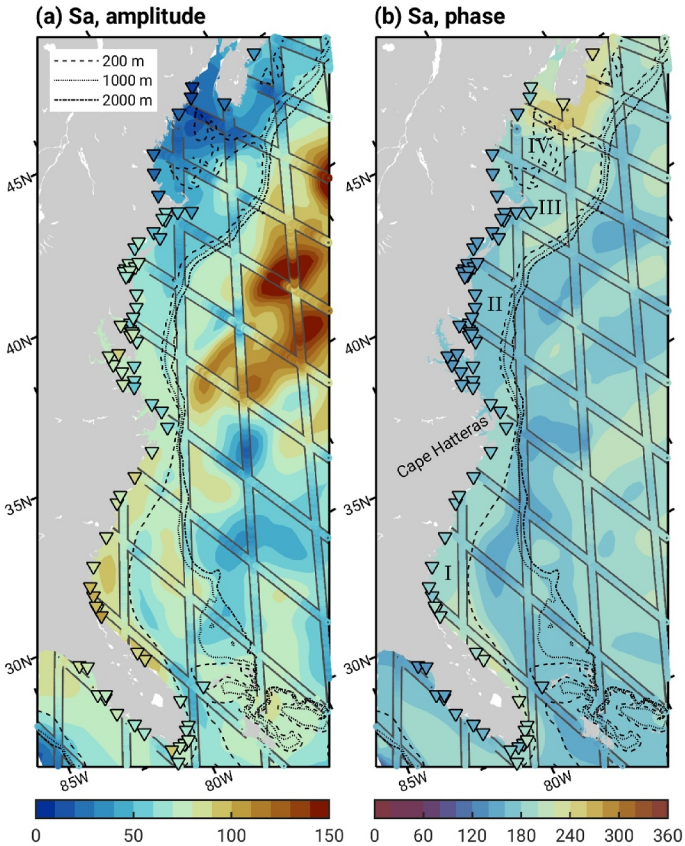

Figure 5. Mean annual sea level cycle (Sa) in (a) amplitude (mm) and (b) phase (deg) along the North American east coast, estimated from DUACS altimetry (filled contours in the background), X-TRACK (circles along the tracks), and tide gauges (triangles). Black contours are selected isobaths as indicated in the legend. As in Figure 1, all data were corrected for the inverted barometer effect, the astronomical tide, the pole tide, and—in the case of tide gauges—the annual cycle in vertical land motion. Roman numbers in (b) denote regions mentioned in the text: South Atlantic Bight (I), Mid-Atlantic Bight (II), Georges Bank (III), Gulf of Maine (IV).

correspondence between tide gauges and nearby altimetry on the eastern and western coasts, consistent with the average statistics in Figure 4. As with the eastern North American coast shown in Figure 5, we find no marked impact of X-TRACK on better resolving coastal signals.

Some of the largest Sa variability occurs around Southeast Asia, particularly in the northern Bay of Bengal and in the Gulf of Thailand (Figure 1). Zooming in on the region (Figure 7) reveals a general tendency for larger tide gauge Sa amplitudes compared to altimetry estimates, most conspicuously along the eastern Malaysian coast and the northern Bay of Bengal. No sizable differences are found for phase values. Although without direct tide gauge observations in Figure 7, we can discern a relatively tight trapping of energy to the coasts of Vietnam and eastern India from the altimetric Sa estimates. For both regions, the trapping is accompanied by a signal trough along the nearby continental slope (especially east of India) and distinct phase transitions between near-shore and offshore locations, pointing to differences in the underlying dynamical regimes and forcing factors (Akhter et al., 2021; Amiruddin et al., 2015). Similar cases of trapped Sa variability—albeit with a less drastic decrease in amplitude over the continental slope—are found elsewhere, including the Norwegian west coast and the northern South China Sea (Figures S4 and S5 in Supporting Information S1).

For all Southeast Asian regions discussed in Figure 7, just as in other areas with variable geometry and shelf extent (see Figures S2–S5 in Supporting Information S1), bottom topography can clearly influence the behavior of the annual cycle. While the very shallow Gulf of Thailand has large Sa amplitudes everywhere, the contrast in both amplitudes and phases between the east and west coast of the Malaysian Peninsula, separated by only ~300 km, is striking (cf. also Amiruddin et al., 2015). These results again indicate different dynamic regimes in regions that likely share similar atmospheric forcing but differ in terms of topography and land-sea distribution.

Arguments brought forth for the case of Sa also largely apply to Ssa. The Gulf of Mexico and the South Atlantic Bight represent examples of coastal regions with relative large Ssa amplitudes and considerable differences between tide gauge and altimeter estimates (Figures 2 and 4). Additional examples (including the Baltic Sea, the East and South China seas, and the Bay of Bengal) are illustrated in Figures S6–S9 in Supporting Information S1. From a zoomed view in Figure 8, we find a tendency for damped Ssa amplitudes over the continental slope, particularly in the Gulf of Mexico, with larger amplitudes (~4–6 cm) in shelf regions and in the deep interior. For most shelves, especially those facing eastward, the altimeter fields, while showing a considerable amplification of Ssa toward the coast, still underestimate the amplitudes observed at tide gauges, often by more than 1 cm. Contrasting with the short-scale features in the amplitude fields, there is generally good agreement between altimeter and tide gauge phase values. In a wider context for the region, semiannual phases are almost constant over all shelves (also further to the north, Figure 2), but they change more substantially across the continental slope, and in the deep interior. Taken together, the selected examples for seasonal oscillations in sea level (Figures 5–8 and Figures S2–S9 in Supporting Information S1) confirm the variety of behaviors and factors governing the seasonal cycle across the coastal zone and the difficulty in finding simple relations between offshore and near-coastal estimates of Sa and Ssa in many regions around the globe.

3.4. Steric and Manometric Contributions

Sea level variability can be related to ζ_s and ζ_m terms, respectively representing the effects of changes in the density and mass of the water column (e.g., Gill & Niller, 1973; Gregory et al., 2019). The breakdown in terms of ζ_s and ζ_m components provides information on the underlying dynamics and forcing of ζ variability and sheds light on the consistency of the in situ and satellite observations used to derive ζ, ζ_s, and ζ_m.

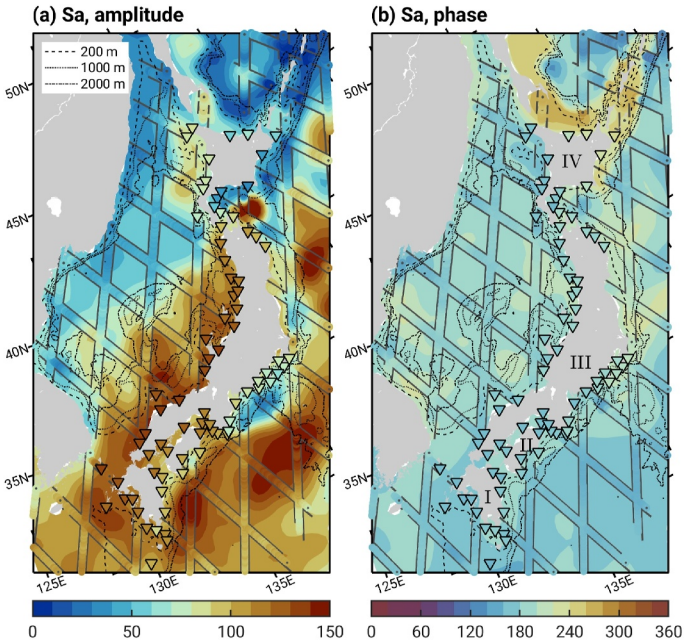

Figure 6. As in Figure 5 but for the annual sea level cycle around Japan. Roman numbers in (b) denote the main Japanese islands mentioned in the text: Kyushu (I), Shikoku (II), Honshu (III), Hokkaido (IV).

In the context of the seasonal cycle in coastal ζ, in principle one expects ζ_s contributions to approach zero as the depth of the water column decreases, so that a tide gauge measuring in very shallow water will be mostly reflecting local changes in ζ_m (Bingham & Hughes, 2012). Nevertheless, such ζ_m changes can partly result from mass transfers associated with heating/cooling and ζ_s changes over deeper waters adjacent to the tide gauge (e.g., Landerer et al., 2007; Ponte et al., 2002; Yin et al., 2010). More generally, the partition in terms of ζ_m and ζ_s will depend on depth and numerous dynamical factors. Pattullo et al. (1955) and Vinogradov et al. (2008) suggest regimes with either ζ_s or ζ_m as important contributors depending on region, but prior to the GRACE mission, no global observations of ζ_m were available. Despite the relatively low resolution of the GRACE fields, studies have called attention to the usefulness of these data in explaining observed coastal ζ variability (e.g., Mu et al., 2019; Piecuch et al., 2018; Wang et al., 2015). However, to our knowledge, a comprehensive analysis of the seasonal cycle in ζ, ζ_s, and ζ_m across the coastal zone has not been attempted. Such analysis is pursued here using the gridded DUACS, WOA23, and GRACE data sets described in Section 2, focusing on areas shallower than 2,000 m, and in relation to the tide gauge estimates.

A quantitative measure of closure and relative importance of each term in the ζ budget is the percentage of variance explained (PVE, e.g., Vinogradov et al., 2008)

$$\mathrm{PVE} = \frac{\sigma_\zeta^2 - \sigma_r^2}{\sigma_\zeta^2} \cdot 100\%, \tag{1}$$

where σ^2 denotes variance and subscript r refers to residual series $\zeta - \zeta_s$, $\zeta - \zeta_m$, or $\zeta - (\zeta_s + \zeta_m)$. A PVE of ~100% implies $\sigma_r^2 \ll \sigma_\zeta^2$, that is, the component tested in the residual series explains nearly all the variance in ζ. Examining first regionally aggregated statistics of PVE for the Sa and Ssa harmonics from tide gauges (Tables 2 and 3), and considering $\zeta_s + \zeta_m$ from nearest neighbor interpolation of ζ_s and ζ_m, we obtain median values ≥50% for all regions examined except both Australian coasts and New Zealand (Sa) and the Gulf of Mexico (Ssa). These values increase moderately for most tabulated regions if one replaces the tide gauge ζ harmonics by the DUACS estimates collocated with those of ζ_s and ζ_m. Thus, aside from data noise, some of the unexplained variance in the tide gauges can be due to differences in the seasonal cycle between the coast and the closest point where ζ_s and ζ_m

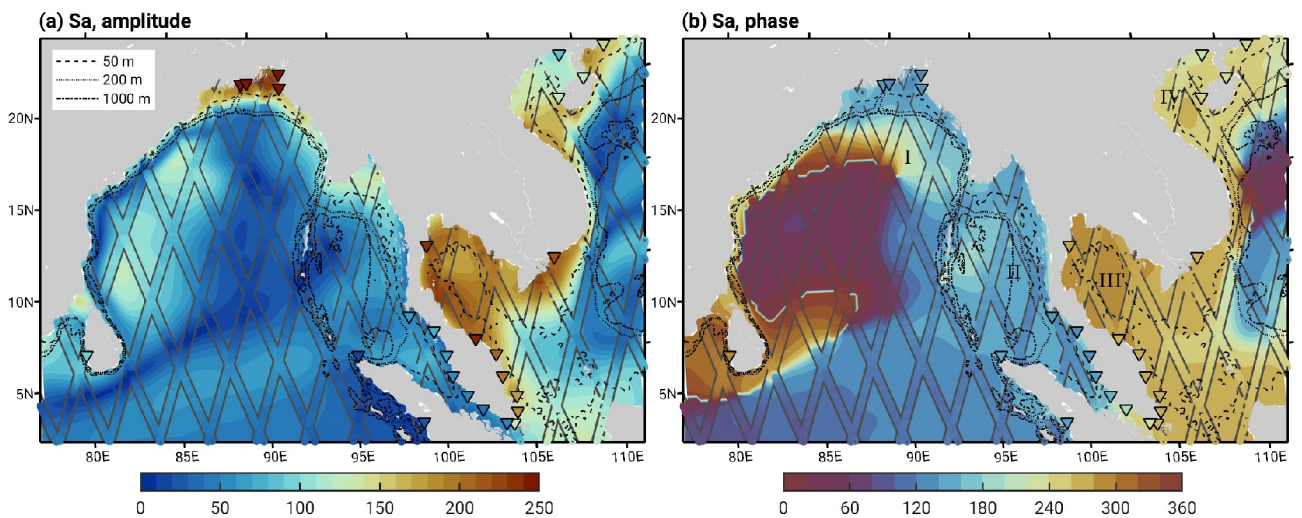

Figure 7. As in Figure 5 but for the annual sea level cycle in the Bay of Bengal (denoted by roman number I in panel b), Andaman Sea (II), Gulf of Thailand (III), and South China Sea, comprising also the Gulf of Tonkin (IV).

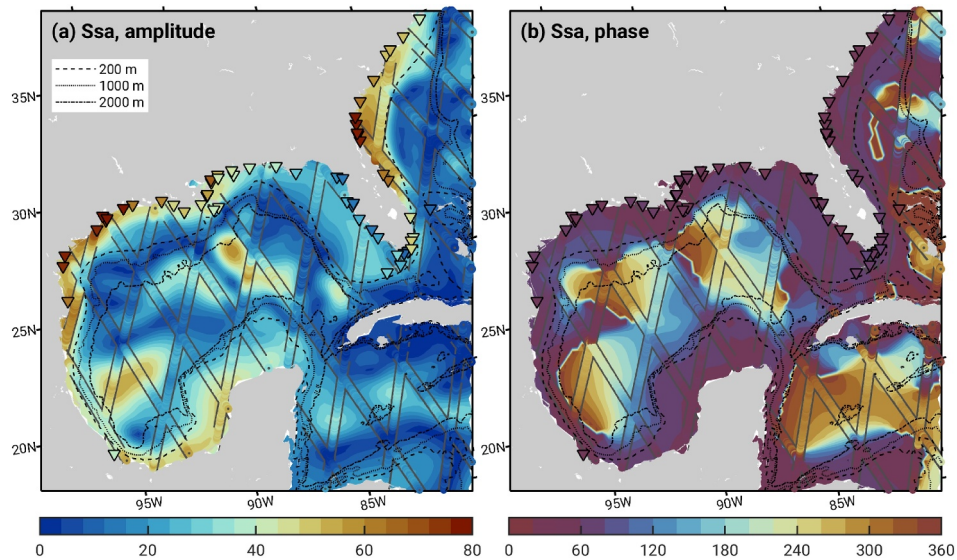

Figure 8. Mean semiannual sea level cycle (Ssa) in (a) amplitude (mm) and (b) phase (deg) in the Gulf of Mexico and the South Atlantic Bight, deduced from altimetry and tide gauges as in Figure 5. All data were corrected for the inverted barometer effect, the astronomical tide, and—in the case of tide gauges—the semiannual cycle in vertical land motion.

Table 2
Budget of the Sa Harmonic in ζ in 13 Selected Coastal Regions From Observations[a,b,c]

	Sa tide gauges		$\zeta_s + \zeta_m$		PVE (%)		
Region	*A* (cm)	*G* (deg)	*A* (cm)	*G* (deg)	ζ_s	ζ_m	$\zeta_s + \zeta_m$
US East (66)	6.5	172	4.0	163	63	30	75 (75)
Gulf of Mexico (38)	7.0	170	4.5	167	28	41	74 (81)
US West (21)	7.2	264	2.2	242	39	3	51 (72)
Andean (16)	0.7	34	1.1	26	65	−30	62 (81)
Northwest European Shelf (113)	7.4	226	4.6	218	8	56	76 (78)
Baltic Sea (45)	6.6	232	3.7	228	−3	58	64 (79)
Mediterranean Sea (31)	6.2	206	2.0	209	57	−48	50 (47)
Japan (79)	10.1	187	10.1	179	94	20	92 (92)
East China Sea (11)	11.3	230	8.4	232	−7	85	86 (87)
Bay of Bengal, Thailand (19)	6.8	218	7.5	272	−0	64	67 (69)
Australia West (16)	10.5	61	4.1	86	16	27	42 (47)
Australia East (32)	6.4	45	2.3	38	9	10	23 (35)
New Zealand (12)	4.5	26	1.1	25	41	−45	36 (45)
Median PVE over 13 regions	–	–	–	–	28	27	64 (75)

[a]Tabulated are mean amplitudes *A* and phases *G* of the annual sea level cycle per region, as observed at tide gauges (columns 2–3) and calculated from WOA23 and GRACE-based estimates of ζ_s and ζ_m (columns 4–5). The last three columns list the median PVE in ζ at tide gauges by ζ_s, ζ_m, and $\zeta_s + \zeta_m$, complemented by median statistics over all 13 regions in the bottom row. Values in parentheses under $\zeta_s + \zeta_m$ are also median PVE in the annual cycle of ζ, but with ζ at a given grid point taken from DUACS instead of the nearest tide gauge. [b]Numbers in parentheses in the leftmost column represent the total count of tide gauges per regional average, see Figure S1 in Supporting Information S1 for their location. [c]Figure S13 in Supporting Information S1 additionally presents a global view of the PVE by ζ_s, ζ_m, and $\zeta_s + \zeta_m$ at all 747 individual tide gauges.

Table 3
Budget of the Ssa Harmonic in ζ in Selected Coastal Regions From Observations[a]

	Ssa tide gauges		$\zeta_s + \zeta_m$		PVE (%)		
Region	A (cm)	G (deg)	A (cm)	G (deg)	ζ_s	ζ_m	$\zeta_s + \zeta_m$
US East (66)	3.8	53	1.3	76	9	45	53 (59)
Gulf of Mexico (38)	4.8	61	1.6	72	−3	38	43 (63)
Baltic Sea (45)	3.1	265	1.7	249	15	44	61 (85)
East China Sea (11)	4.3	49	2.9	70	15	61	74 (86)
Bay of Bengal, Thailand (19)	4.7	138	4.2	156	11	64	75 (71)
Australia West (16)	2.8	129	1.2	130	3	43	54 (52)
Median PVE over 13 regions	–	–	–	–	7	43	43 (41)

[a]Statistics as in Table 2 but only for regions with average Ssa amplitudes >2.5 cm in tide gauges. The last row lists median statistics over all 13 regions and Figure S14 in Supporting Information S1 shows the PVE in Ssa by ζ_s, ζ_m, and $\zeta_s + \zeta_m$ at individual tide gauges.

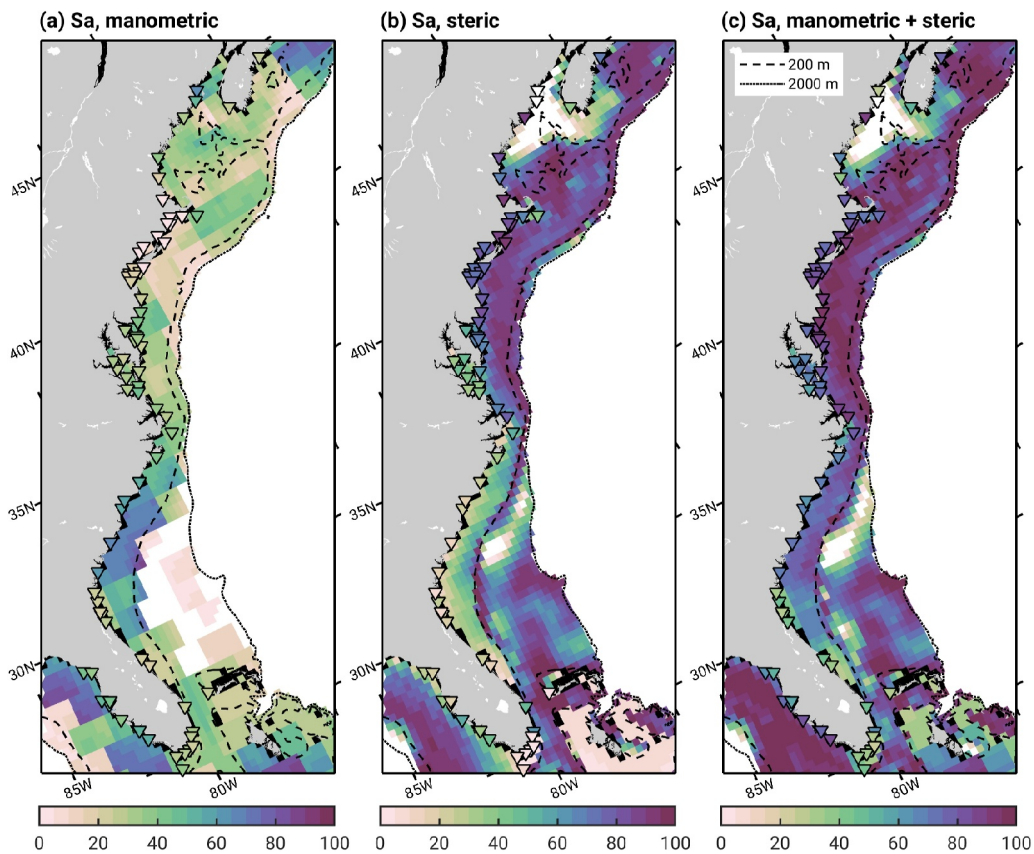

Figure 9. Attribution of the annual cycle in sea level to steric and manometric components along the North American east coast. Shown are estimates for the PVE in tide gauge and DUACS Sa harmonics by (a) ζ_m from GRACE, (b) ζ_s from WOA23, and (c) the sum $\zeta_s + \zeta_m$. Negative PVE and values in the deep ocean (>2,000 m) are clipped.

10.1029/2024EA003978

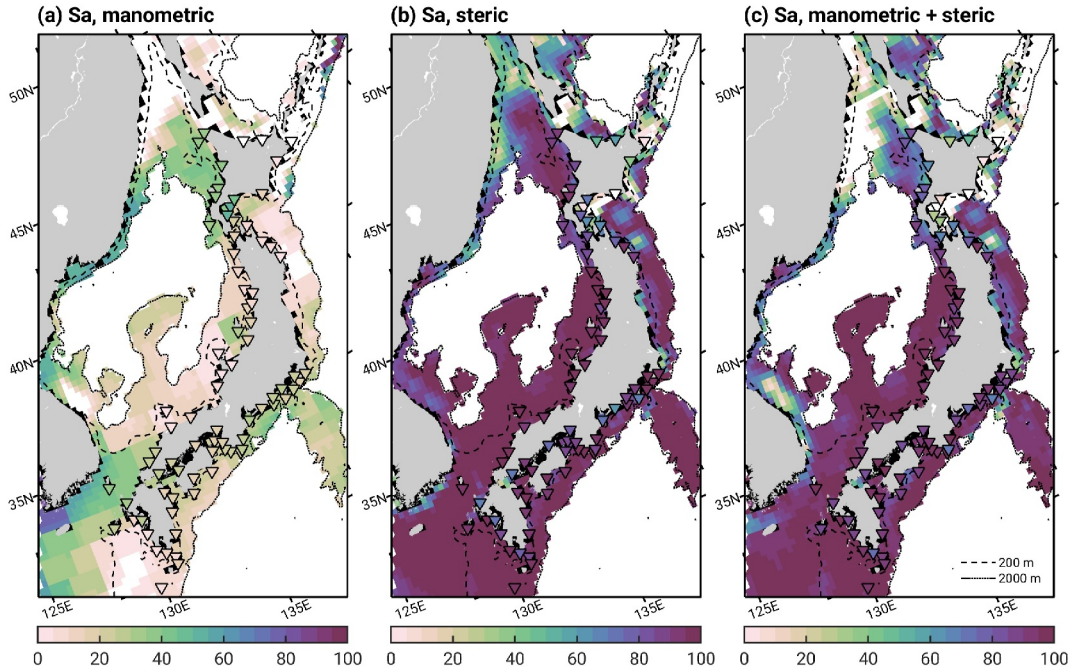

Figure 10. As in Figure 9 but for the annual sea level cycle around Japan and in the Japan/East Sea.

data are available. Importantly, most regions (except, for example, the Andean coast and Mediterranean Sea) show improved budget closure when considering $\zeta_s + \zeta_m$ compared to each term individually. Moreover, various behaviors are evident across the different regions: Budgets for Sa (Table 2) can be dominated by either ζ_s or ζ_m, or have similar contributions from both terms, whereas ζ_m clearly governs variability in Ssa (Table 3). For an expanded look at the relation between ζ, ζ_s and ζ_m fields, we focus on some of the regions already examined in Section 3.3 and map PVE statistics across the coastal zone.

For the annual cycle near the US east coast (Figure 9), budget closure is somewhat better north of Cape Hatteras (PVE ≥85%), with the exception of the Gulf of Maine where Sa amplitudes are fairly weak (≤3 cm, Figure 5). The importance of ζ_s is clear over much of the wide shelves of the Mid-Atlantic Bight and also Georges Bank. South of Cape Hatteras, a more balanced influence of ζ_s and ζ_m is apparent, although PVE values for $\zeta_s + \zeta_m$ rarely exceed 80% and drop to ~40% along the Florida east coast. One interesting aspect in Figure 9 is the enhanced contribution of ζ_s following the shelf break near the 200-m depth contour, suggestive of the annual migration of the Shelfbreak Jet position and the influence of the Gulfstream along the Mid-Atlantic and South Atlantic Bights, respectively (e.g., Forsyth et al., 2020; Yuan et al., 2017). The wide shelves west of Florida, partly included in Figure 9, reveal excellent budget closure, with ζ signals again attributable to both ζ_s and ζ_m, but with ζ_s (ζ_m) clearly losing (gaining) in importance closer to the coast, as expected. A few exceptions aside, the tide gauge PVE values are similar to the nearby PVE based on the DUACS ζ fields, consistent with results in Table 2.

Tide gauges around Japan exhibit the best ζ budget closure for Sa on average, with a dominant contribution from ζ_s (PVE = 94%; Table 2). Steric expansion thus accounts for almost all of the annual ζ fluctuations apparent in Figure 6, amounting to ~8 cm (~12 cm) in amplitude on the east (west) coast of Japan; see also Feng et al. (2015). The relatively small contributions by ζ_m to the ζ Sa variance are consistent with the narrow shelves of the region, which are likely not well resolved in the GRACE observations. Apart from being weaker (by a factor of about 7), ζ_m estimates, when combined with ζ_s, tend to decrease the PVE values obtained using ζ_s alone. This behavior is particularly noticeable in the western and northern parts of the Japan/East Sea (Figure 10), hinting at noisy or erroneous ζ_m values. Such inference is in accord with the estimates of uncertainty in ζ_m contemplated in Section 4 below; Ponte et al. (2024) also report relatively large uncertainty of GRACE-based annual ζ_m estimates in the coastal areas of the Japan/East Sea (cf. their Figures 1 and 9).

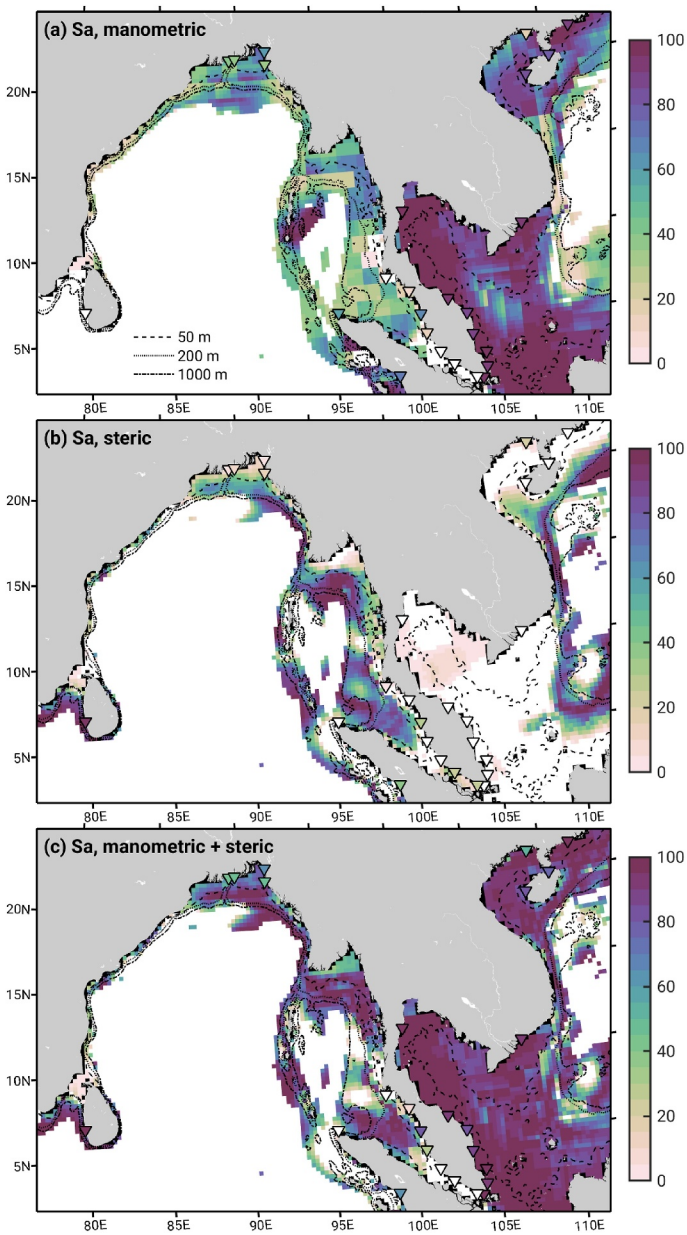

Figure 11. As in Figure 9 but for the annual sea level cycle in the Bay of Bengal, Andaman Sea, Gulf of Thailand, and South China Sea.

The Southeast Asia region treated earlier in Section 3.3 (Figure 7) offers a contrasting picture to that in Figure 10, revealing a dominant role for ζ_m in the annual ζ cycle in the Gulf of Thailand and also over much of the South China Sea (Figure 11). Except for the impact of ζ_s near the Vietnamese coast and the inner Gulf of Tonkin, the PVE values associated with ζ_m are >80% across most of these areas. Apart from being very shallow (<200 m, with large parts <50 m), the region is primarily forced by monsoonal winds that favor large seasonal ζ_m anomalies and mass redistribution within the focus area (Qu et al., 2022; Saramul & Ezer, 2014). In the coastal areas of the Bay of Bengal and Andaman Sea, both ζ_m and ζ_s contribute to the annual ζ cycle, explaining also considerable fractions of the large (≥20-cm) Sa amplitudes in the DUACS altimetry near the Ganges-Brahmaputra delta (Figure 7a). Nonetheless, the ζ budget in these areas is not nearly as closed as that in the Gulf of Thailand and South China Sea, in part due to generally weaker Sa signals. In addition, it is plausible that the quality of both ζ_m and ζ_s suffers from poor data sampling, including inadequate spatial resolution across the narrow Indian shelf, or, in the case of ζ_m, residual errors in the separation of mass change signals from terrestrial and oceanic sources (cf. Scanlon et al., 2016, especially their Figure 12).

Turning again to Tables 2 and 3, our budget evaluations underscore the importance of ζ_m for the semiannual ζ cycle. Variability in ζ_s is still partly connected to the Ssa signals seen at the coast, particularly in regions of notable Ssa amplitudes such as the Bay of Bengal Shelf (Figure S8 in Supporting Information S1) and the western Gulf of Mexico (Figures 8 and 12). Nevertheless, gridded PVE values for the Gulf of Mexico in Figure 12 mainly highlight the near-shore impact of semiannual ζ_m signals, for example, on the West Florida Shelf (ζ_m amplitude ~2.5 cm) and the Texas-Louisiana Shelf (ζ_m amplitude ~3.5 cm). In any case, throughout most of the tested coasts—including those in the Gulf of Mexico, the South Atlantic Bight, western Australia (Figure S12 in Supporting Information S1) and other areas listed in Table 3—semiannual variability in ζ_m and ζ_s does only partially represent the ζ Ssa signals observed by the tide gauges. Specifically, when taking the median PVE values for $\zeta_s + \zeta_m$ over all 13 predefined regions, we obtain an aggregated budget closure statistic of 43% for Ssa (Table 3), compared to 64% for Sa (Table 2).

Figure 13 presents a condensed view of the partitioning of seasonal ζ variability into ζ_m and ζ_s and its dependence on depth, touched on above in relation to Figures 9–12. For most of the selected regions (demarcated in Figure S1 in Supporting Information S1), ζ_s amplitudes tend to decrease with depth, contrasting with the opposite tendency of seasonal ζ_m amplitudes, most evident at depths <100 m. More generally, the increase in ζ_m values toward very shallow water mimics the behavior of the altimetric ζ amplitudes, clearly seen over the wide shelves of the Gulf of Thailand (cf. Figures 7 and 11), the Northwest European Shelf (Figures S3 and S10 in Supporting Information S1), or the East China and Yellow seas (Figures S5 and S11 in Supporting Information S1). An exception is the annual cycle in the Mediterranean Sea (Figure 13d), where ζ_m Sa amplitudes are virtually independent of depth. This result is consistent with the presence of a basin-scale mode of near-uniform ζ_m variability that is commonly associated with the response to wind stress fluctuations at and near the Strait of Gibraltar (Fukumori et al., 2007). Overall, while ζ_m plays an increasingly important role in the seasonal cycle in ζ in shallower coastal regions, comparisons of the various quantities in Figure 13 (ζ_m, ζ_s, ζ from altimetry and tide gauges) confirm that the effects of ζ_s cannot be neglected even in close proximity to the coasts.

10.1029/2024EA003978

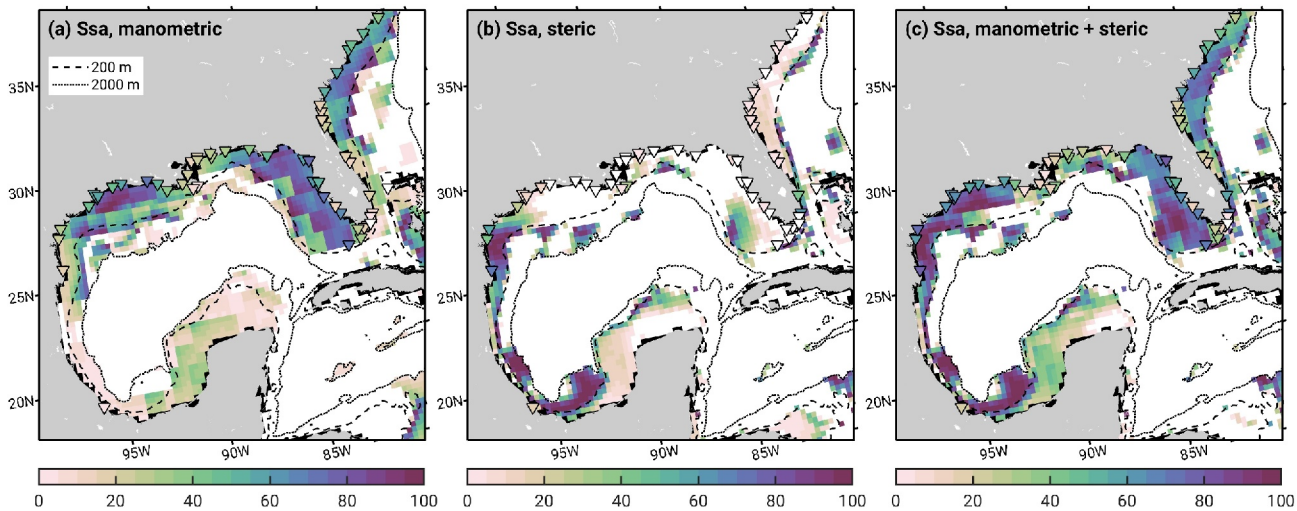

Figure 12. As in Figure 9 but for the semiannual sea level cycle in the Gulf of Mexico and South Atlantic Bight.

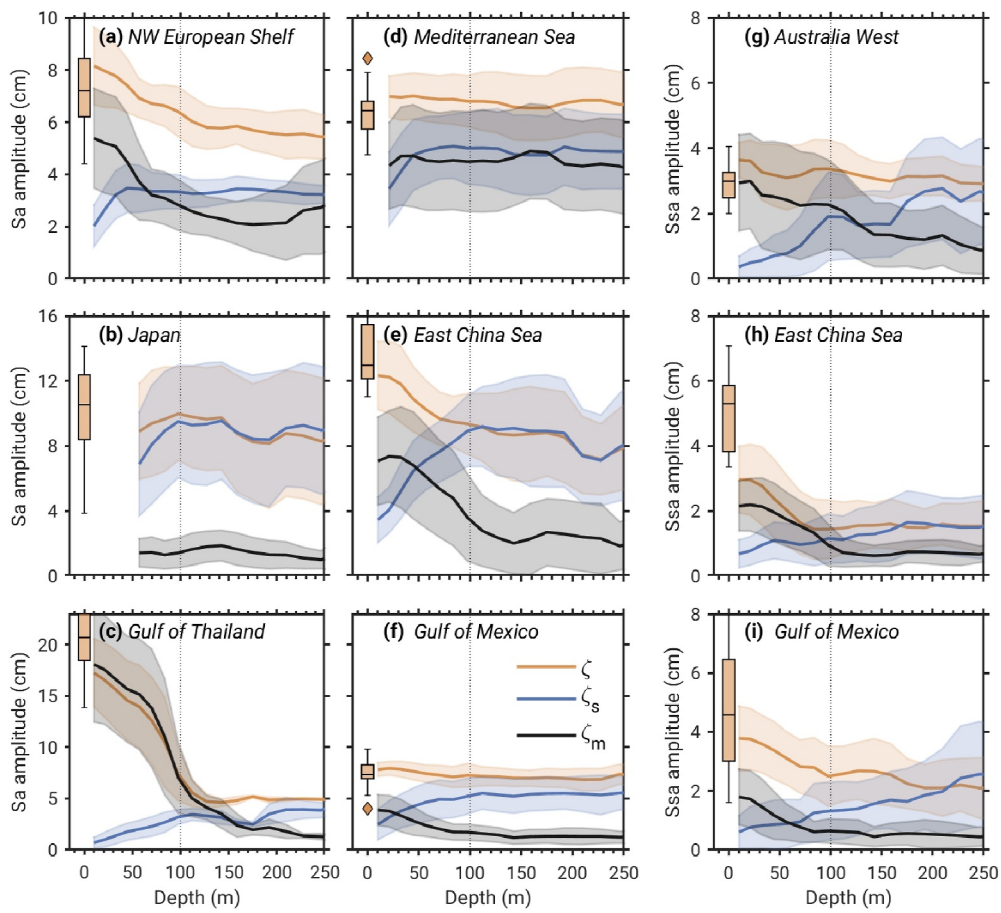

Figure 13. (a)–(f)Amplitudes of ζ from DUACS (cream), ζ_s (blue), and ζ_m (black) as a function of depth, averaged over regions listed on each panel, for the case of (a)–(f) Sa and (g)–(i) Ssa. Solid lines and shading represent mean values and onefold standard deviations per averaging bin, with bin widths increasing linearly toward deeper water from 20 m to about 40 m across the plotted depth range. Values in near-coastal bins with less than 50 grid cells are excluded; cf. panels (b) and (d). The boxplot values at 0 m summarize the ζ amplitude statistics observed by the tide gauges for each respective region and harmonic.

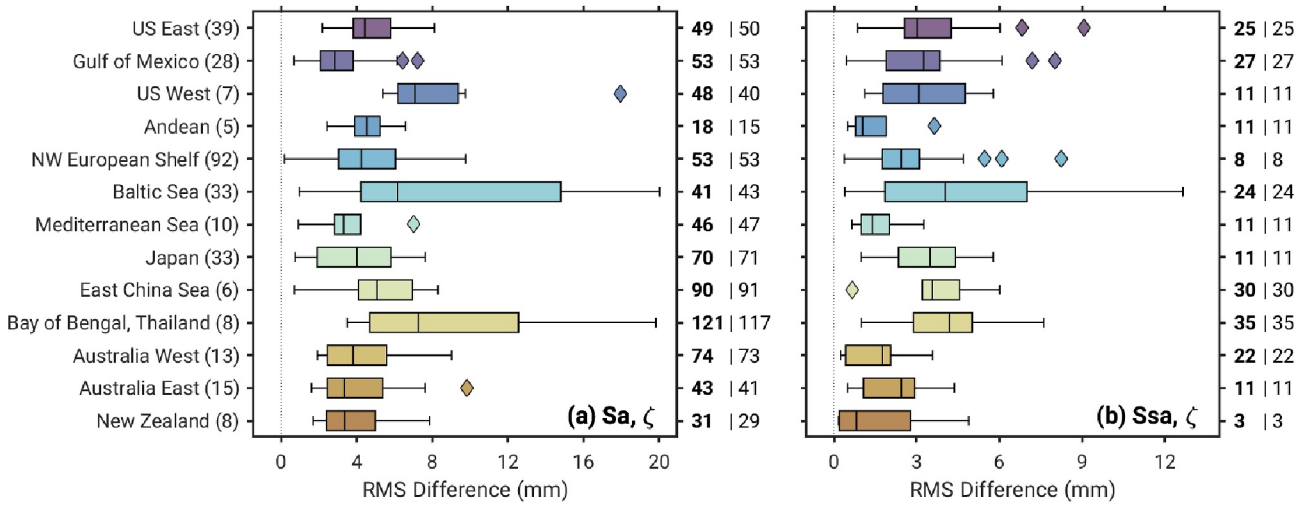

Figure 14. Boxplot of RMS differences (mm) between X-TRACK and DUACS estimates of the seasonal ζ cycle (Sa, Ssa) in the 13 coastal regions analyzed elsewhere in this work. The DUACS values were linearly interpolated to the X-TRACK along-track locations before averaging the respective harmonics in the vicinity (70-km radius, depth <200 m) of available tide gauges. Numbers in parentheses next to the region names show the total count of data points per region. Numbers on the right vertical axis of panels (a) and (b) indicate the harmonic's mean signal (as defined in Table 1) in X-TRACK data (bold font) and DUACS (normal font).

4. Assessment of Uncertainties

In assessing and interpreting differences between tide gauges and altimeter estimates of the seasonal cycle in ζ, and similarly for the budget analysis drawing on corresponding values of ζ_m and ζ_s, it is useful to have estimates of uncertainty, even if very approximate, for the different variables. To attempt such an analysis of uncertainty, we choose to compare different estimates of ζ, ζ_m, and ζ_s and calculate respective RMS differences. For ζ, we use differences between X-TRACK and DUACS; for ζ_m and ζ_s, the GRACE and WOA23 observations are assessed against corresponding values from ORAS5.

The ζ statistics, summarized in Figure 14 for our 13 tide gauge clusters, reveal median RMS differences $\sim$8 mm for Sa and $\sim$5 mm for Ssa. Full range of RMS differences, including outliers, is typically much smaller than the RMS signal of the observed Sa and Ssa harmonics. Regions with weakest signal-to-noise ratios include the Baltic Sea for both Sa and Ssa, and the Northwest European Shelf and New Zealand for Ssa, where mean signals do no exceed 10 mm. The RMS differences between X-TRACK and DUACS estimates in Figure 14 are of the same order of magnitude but somewhat smaller than those between the two altimeter products and the tide gauges in Table 1. Assuming the tide gauge estimates have negligible uncertainties compared to the altimeter products (cf. also Section 2.1), one can thus infer that the differences between tide gauges and the latter fields discussed in Sections 3.1 and 3.3 are at least partially due to the effects of short-scale features present within a few kilometers of the coastline.

Estimates of uncertainty for ζ_s and ζ_m (Figure 15) imply typically smaller signal-to-noise ratios than those of ζ. For ζ_s, uncertainties in Sa are mostly $\sim$15 mm and considerably smaller than the signal amplitudes, except at Southeast Asian tide gauges (Figure 15a); results for Ssa indicate low ζ_s signal-to-noise ratios in part because of the very weak (essentially sub-centimeter) signals (Figure 15b). The RMS differences between GRACE and ORAS5 suggest ζ_m is the most uncertain component in our realization of the sea level budget. Focusing on Sa, which is much stronger than Ssa, many of the regions highlighted in Figure 15c show signals in the GRACE solutions to be substantially smaller than those from ORAS5, by about 35% on average but more in several cases (e.g., US east coast). RMS differences are thus comparable in size with the GRACE signals themselves. One notable exception is the Bay of Bengal/Thailand region, where ζ_m contributions to the Sa harmonic in ζ are large and good budget closure is observed particularly in the Gulf of Thailand (Figure 11).

Given the orbital configuration of GRACE (i.e., altitude, repeat cycle, inter-satellite distance) and the nature of the geophysical inversion process (Chen et al., 2022; Swenson & Wahr, 2002), monthly gravity field solutions nominally resolve surface mass changes such as ζ_m to spatial scales of a few hundred kilometers. Use of

10.1029/2024EA003978

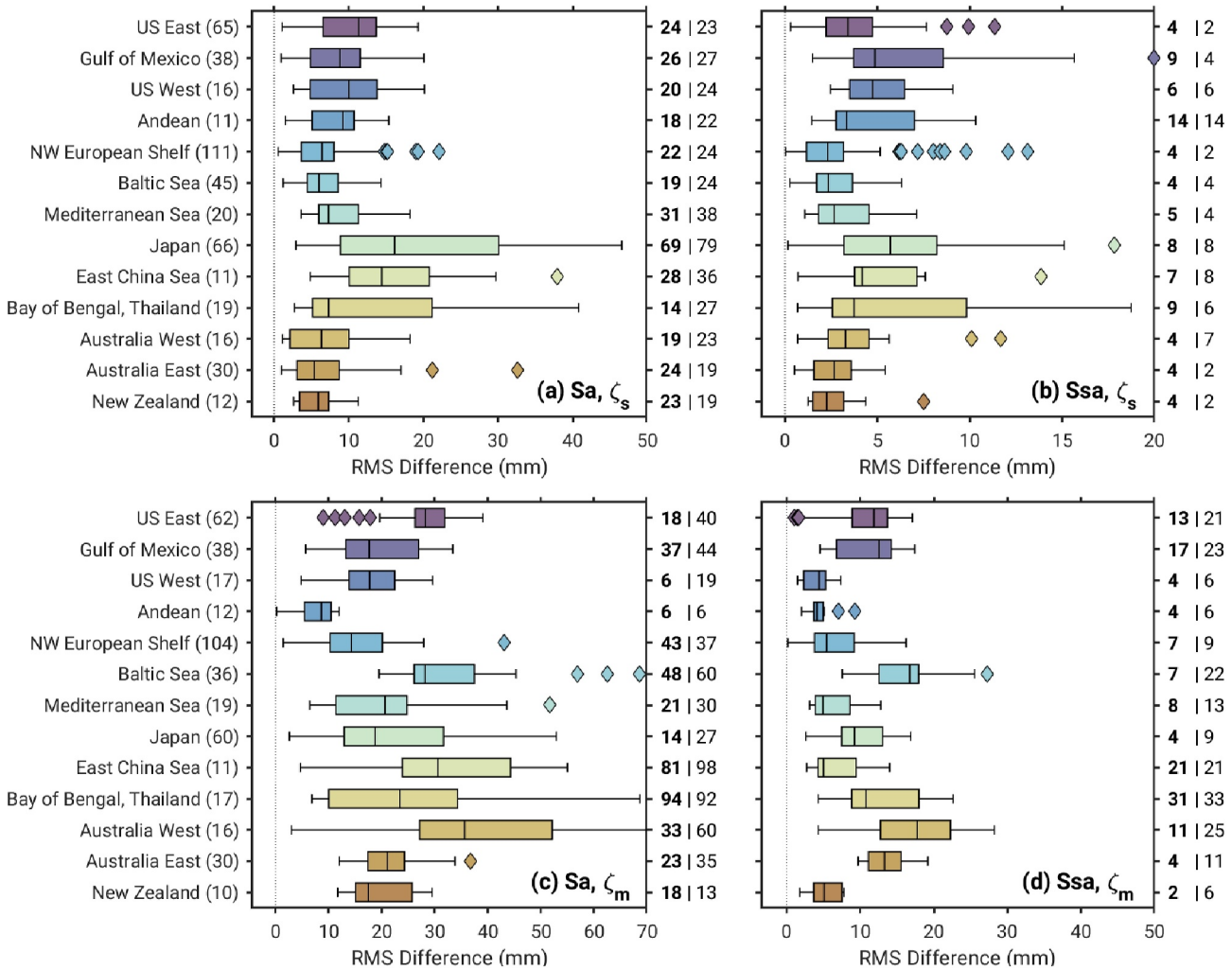

Figure 15. Boxplot of Sa and Ssa RMS differences (mm) in 13 coastal regions, similar to Figure 14, but for (a), (b) comparisons of ζ_s harmonics from WOA23 and ORAS5, and (c), (d) comparisons of ζ_m harmonics from GRACE and ORAS5. The data points considered per region (number in parentheses on the left) are all available shallow (<200 m) 1/4° grid cells within 70 km from a tide gauge. Numbers on the right vertical axes indicate the respective harmonic's mean signal from WOA23 (bold font, top row), GRACE (bold font, bottom row), and ORAS5 (normal font).

constraints on mass variability in time and space, as done for mascons, can help refine the resolution (or more precisely, the grid spacings) to ~1° × 1° (Loomis et al., 2019; Save et al., 2016). However, long-range spatial correlations up to ~3° may still be present in these solutions (Loomis et al., 2019; Watkins et al., 2015). Figure 16 illustrates the limits in resolution of the mascon-based ζ_m estimates used in our work by zooming in on Australia and comparing the Sa amplitude with that derived from ORAS5 (1/4° grid). Evidently, the GRACE estimate agrees with ORAS5 roughly at the scale of the adopted mascons but fails to capture the amplitude increase within 50–100 km from the shore—a salient feature along the East, West, and South Australian coasts. Moreover, Sa amplitudes in the Gulf of Carpentaria are ~50% smaller than in the reanalysis and point to strong signal losses in the inversion of the southernmost, coastal mascons. In additional analyses (not shown), we have tested another 1° GRACE mascon product (Save et al., 2016) and obtained somewhat better agreement with ORAS5 and tide gauges in a few regions, including East and West Australia. However, regionally condensed statistics for both harmonics in ζ_m were very similar to those in Figures 15c and 15d, supporting the idea that resolution of current GRACE products is a detrimental factor in the ζ budget analysis attempted in Tables 2 and 3 and Figures 9–13.

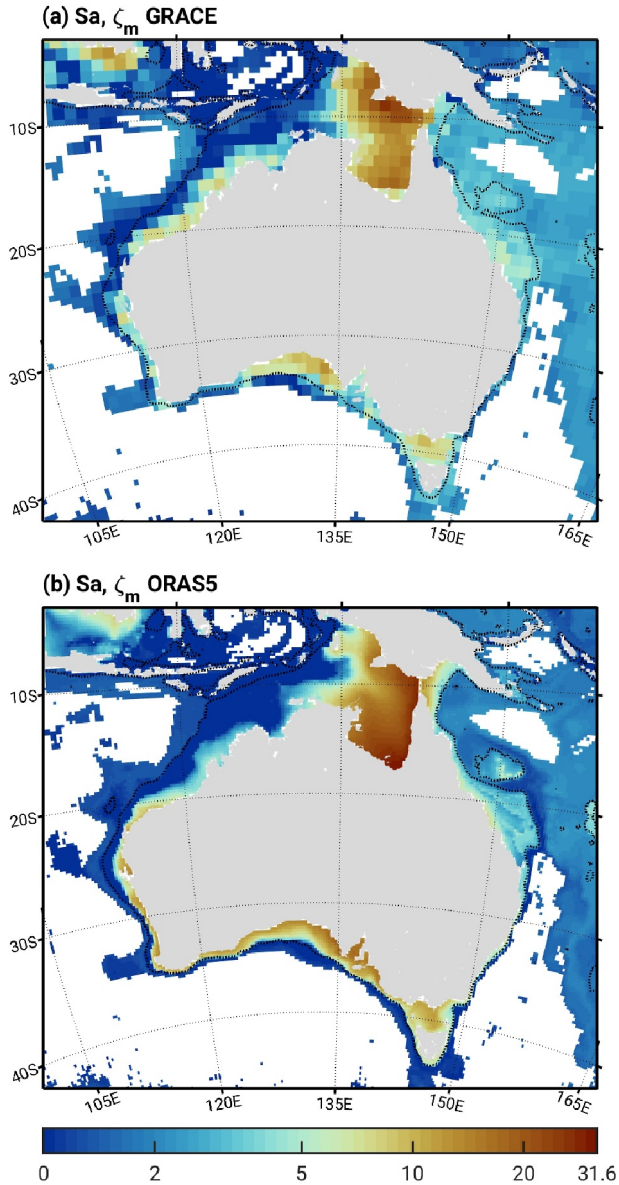

Figure 16. Manometric Sa amplitude (cm) around Australia as deduced from (a) GRACE-based estimates of ζ_m given as 1° mascons, and (b) ORAS5 ζ_m fields on a 1/4° × 1/4° grid. Regions deeper than 4,000 m are clipped and the dashed contour indicates the 1,000-m isobath. Note the non-linear color scale for amplitudes.

5. Summary and Final Considerations

The mean seasonal cycle in ζ is a distinct target signal for understanding ocean dynamics (e.g., Amiruddin et al., 2015; Gill & Niller, 1973; Hochet et al., 2024; Vinogradov et al., 2008) and testing for progress in coastal sea level monitoring (Passaro et al., 2015; Ray et al., 2021; Ruiz Etcheverry et al., 2015; Vinogradov & Ponte, 2010). We have revisited the subject by adopting a near-global scale perspective on coastal transition zones, as sampled by tide gauges, satellite altimeters, the GRACE/-Follow On missions, and hydrographic observations. The mean seasonal ζ cycle, extracted from approximately three decades of sea level data, displays a rich spatial structure both along and across the coastal zones, with the annual term generally larger than the semiannual term. Sizable differences remain between tide gauge and altimeter Sa and Ssa estimates, even when using altimeter products specifically tailored for coastal applications. Smallest RMS differences (Table 1, Figures 3 and 4) are typically larger than the respective oscillation's ζ uncertainty, quantified based on differences between gridded and along-track altimeter products (Figure 14). Our results indicate that appreciable changes in the mean seasonal cycle can be present within a few kilometers of the tide gauges in numerous regions of the global ocean.

We have also explored the nature of the ζ seasonal budget in several well-instrumented regions (depths <2000 m), drawing on ζ_s and ζ_m estimates deduced from monthly climatologies of temperature and salinity (WOA23) and GRACE gravity field solutions. On average, the sum $\zeta_s + \zeta_m$ can account for ~2/3 of the observed annual ζ variance at tide gauges, but results vary with region (Table 2, Figures 9–11) and sometimes even among neighboring sites (Figure S13 in Supporting Information S1). In areas with good Sa budget closure, comprising, for example, Japan and the Northwest European Shelf, both ζ_m and ζ_s can be important, with contributions from ζ_m generally increasing with shallowing depths (Figure 13). The attribution of coastal Ssa variability to steric and manometric components is less successful than for Sa (Table 3, Figures 12 and 14) and evidently inhibited by low signal-to-noise ratios in ζ_s and ζ_m (Figure 15). For both harmonics, comparisons with an ocean reanalysis (ORAS5) suggest that GRACE-based ζ_m estimates have limited ability to represent short-scale variations of the seasonal cycle near the coasts (Figures 15 and 16). Similar issues can affect the ζ_s climatologies from WOA23, given the limited in situ temperature and salinity observations over most shallow coastal regions (e.g., Marcos et al., 2019; Sun et al., 2019).

Ultimately, our analysis of the mean seasonal cycle points to the need for improved spatial resolution of observations of sea level, and its steric and manometric components, to properly characterize the ζ variability across the coastal ocean. Achieving finer horizontal scales in estimates of ζ_m is indeed a key objective of future satellite gravimetry missions (Daras et al., 2024) and also underlies ongoing efforts to downscale the nominal GRACE mascon products in a physically meaningful way (Gou et al., 2024). Regarding ζ itself, the Surface Water Ocean Topography satellite mission promises to bring unprecedented spatial resolution to near-coastal sea level retrievals (Fu et al., 2024). Such a space-based tide gauge will advance the present ability to quantify ζ variability at the coast, where it matters most for addressing societal needs, particularly in the extensive regions currently devoid of in situ tide gauge measurements.

Data Availability Statement

The analyzed seasonal harmonics in ζ (DUACS, MEaSUREs, X-TRACK, tide gauges), ζ_m, ζ_s, and corrective quantities of Section 2.3 are provided in Schindelegger et al. (2024). For the original data sets see the following links: GESLA-3 tide gauge records (https://www.gesla.org/, Haigh et al., 2022), WOA23 (https://www.ncei.noaa.gov/access/world-ocean-atlas-2023/, Reagan et al., 2024), GSFC global mascon solutions (https://earth.gsfc.nasa.gov/geo/data/grace-mascons, Loomis et al., 2019), and ORAS5 reanalysis output (https://doi.org/10.48670/moi-00024, Zuo et al., 2017). The X-TRACK-L2P data used in this study (v2.1, doi: 10.24400/527896/a01-2022.020) were developed, validated by the CTOH/LEGOS, France and distributed by Aviso+.

Acknowledgments

This work was supported by Grants OCE-2239805 (NSF Physical Oceanography Program) and 80NSSC24K1154 (NASA GRACE Follow-On Science Team) to AER. M.S. was supported by the German Research Foundation (DFG, Project no. 388296632). The authors thank Anara Kudabayeva for her initial analysis of the seasonal cycle in X-TRACK data, Lara Börger for help with processing the ORAS5 fields, and Makan Karegar for pointers to vertical land motion literature. The authors are particularly indebted to Richard Ray for making available his gridded DUACS and MEaSUREs harmonics and related geophysical corrections. The color-vision deficiency friendly color schemes used in this work are from Crameri et al. (2020) and Green (2011). Comments by two anonymous reviewers are greatly appreciated. Open Access funding enabled and organized by Projekt DEAL.

References

Akhter, S., Qiao, F., Wu, K., Yin, X., Chowdhury, K. A., & Chowdhury, N. U. M. K. (2021). Seasonal and long-term sea-level variations and their forcing factors in the northern Bay of Bengal: A statistical analysis of temperature, salinity, wind stress curl, and regional climate index data. *Dynamics of Atmospheres and Oceans*, *95*, 101239. https://doi.org/10.1016/j.dynatmoce.2021.101239

Amiruddin, A. M., Haigh, I. D., Tsimplis, M. N., Calafat, F. M., & Dangendorf, S. (2015). The seasonal cycle and variability of sea level in the South China Sea. *Journal of Geophysical Research: Oceans*, *120*(8), 5490–5513. https://doi.org/10.1002/2015JC010923

Bingham, R. J., & Hughes, C. W. (2012). Local diagnostics to estimate density-induced sea level variations over topography and along coastlines. *Journal of Geophysical Research*, *117*(C1), C01013. https://doi.org/10.1029/2011JC007276

Birol, F., Fuller, N., Lyard, F., Cancet, M., Niño, F., Delebecque, C., et al. (2017). Coastal applications from nadir altimetry: Example of the X-TRACK regional products. *Advances in Space Research*, *59*(4), 936–953. https://doi.org/10.1016/j.asr.2016.11.005

Birol, F., Léger, F., Passaro, M., Cazenave, A., Niño, F., Calafat, F. M., et al. (2021). The X-TRACK/ALES multi-mission processing system: New advances in altimetry towards the coast. *Advances in Space Research*, *67*(8), 2398–2415. https://doi.org/10.1016/j.asr.2021.01.049

Börger, L., Schindelegger, M., Dobslaw, H., & Salstein, D. (2023). Are ocean reanalyses useful for Earth rotation research? *Earth and Space Science*, *10*(3), e2022EA002700. https://doi.org/10.1029/2022EA002700

Bruni, S., Fenoglio, L., Raicich, F., & Zerbini, S. (2022). On the consistency of coastal sea-level measurements in the Mediterranean Sea from tide gauges and satellite radar altimetry. *Journal of Geodesy*, *96*(6), 41. https://doi.org/10.1007/s00190-022-01626-9

Carrère, L., & Lyard, F. (2003). Modeling the barotropic response of the global ocean to atmospheric wind and pressure forcing - Comparisons with observations. *Geophysical Research Letters*, *30*(6), 1275. https://doi.org/10.1029/2002GL016473

Cazenave, A., Gouzenes, Y., Lancelot, L., Birol, F., Legér, F., Passaro, M., et al. (2023). New network of virtual altimetry stations for measuring sea level along the world coastlines. *SEANOE*. https://doi.org/10.17882/74354

Chanard, K., Métois, M., Rebischung, P., & Avouac, J.-P. (2020). A warning against over-interpretation of seasonal signals measured by the Global Navigation Satellite System. *Nature Communications*, *11*(1), 1375. https://doi.org/10.1038/s41467-020-15100-7

Chen, J., Cazenave, A., Dahle, C., Llovel, W., Panet, I., Pfeffer, J., & Moreira, L. (2022). Applications and challenges of GRACE and GRACE Follow-On satellite gravimetry. *Surveys in Geophysics*, *43*(1), 305–345. https://doi.org/10.1007/s10712-021-09685-x

Cheng, X., & Qi, Y. (2010). On steric and mass-induced contributions to the annual sea-level variations in the South China Sea. *Global and Planetary Change*, *72*(3), 227–233. https://doi.org/10.1016/j.gloplacha.2010.05.002

Codiga, D. L. (2011). Unified tidal analysis and prediction using the UTide Matlab functions (Tech. Rep. No. 2011-01). *Graduate School of Oceanography, University of Rhode Island Narragansett, RI*. https://doi.org/10.13140/RG.2.1.3761.2008

Crameri, F., Shephard, G. E., & Heron, P. J. (2020). The misuse of colour in science communication. *Nature Communications*, *11*(1), 5444. https://doi.org/10.1038/s41467-020-19160-7

Daras, I., March, G., Pail, R., Hughes, C. W., Braitenberg, C., Güntner, A., et al. (2024). Mass-change and Geosciences International Constellation (MAGIC) expected impact on science and applications. *Geophysical Journal International*, *236*(3), 1288–1308. https://doi.org/10.1093/gji/ggad472

Dee, D. P., Uppala, S. M., Simmons, A. J., Berrisford, P., Poli, P., Kobayashi, S., et al. (2011). The ERA-Interim reanalysis: Configuration and performance of the data assimilation system. *Quarterly Journal of the Royal Meteorological Society*, *137*(656), 553–597. https://doi.org/10.1002/qj.828

Desai, S., Wahr, J., & Beckley, B. (2015). Revisiting the pole tide for and from satellite altimetry. *Journal of Geodesy*, *89*(12), 1233–1243. https://doi.org/10.1007/s00190-015-0848-77

Dobslaw, H., Bergmann-Wolf, I., Dill, R., Poropat, L., & Flechtner, F. (2017). *Product description document for AOD1B release 06, rev. 6.1*. GFZ Potsdam. Retrieved from ftp://isdcftp.gfz-potsdam.de/grace/DOCUMENTS/Level-1/GRACE_AOD1B_Product_Description_Document_for_RL06.pdf. Accessed 14 June 2024.

Dong, D., Fang, P., Bock, Y., Cheng, M. K., & Miyazaki, S. (2002). Anatomy of apparent seasonal variations from GPS-derived site position time series. *Journal of Geophysical Research*, *107*(B4). https://doi.org/10.1029/2001JB000573

Doodson, A. T. (1928). VI. The analysis of tidal observations. *Philosophical Transactions of the Royal Society of London - Series A: Containing Papers of a Mathematical or Physical Character*, *227*, 223–279. https://doi.org/10.1098/rsta.1928.0006

Feng, X., Tsimplis, M. N., Marcos, M., Calafat, F. M., Zheng, J., Jordà, G., & Cipollini, P. (2015). Spatial and temporal variations of the seasonal sea level cycle in the northwest Pacific. *Journal of Geophysical Research: Oceans*, *120*(10), 7091–7112. https://doi.org/10.1002/2015JC011154

Forsyth, J., Andres, M., & Gawarkiewicz, G. (2020). Shelfbreak Jet structure and variability off New Jersey using ship of opportunity data from the CMV Oleander. *Journal of Geophysical Research: Oceans*, *125*(9), e2020JC016455. https://doi.org/10.1029/2020JC016455

Fu, L.-L. (2007). Intraseasonal variability of the equatorial Indian Ocean observed from sea surface height, wind, and temperature data. *Journal of Physical Oceanography*, *37*(2), 188–202. https://doi.org/10.1175/JPO3006.1

Fu, L.-L., Pavelsky, T., Cretaux, J.-F., Morrow, R., Farrar, J. T., Vaze, P., et al. (2024). The Surface Water and Ocean Topography mission: A breakthrough in radar remote sensing of the ocean and land surface water. *Geophysical Research Letters*, *51*(4), e2023GL107652. https://doi.org/10.1029/2023GL107652

Fukumori, I., Menemenlis, D., & Lee, T. (2007). A near-uniform basin-wide sea level fluctuation of the Mediterranean Sea. *Journal of Physical Oceanography*, *37*(2), 338–358. https://doi.org/10.1175/JPO3016.1

Gill, A., & Niller, P. (1973). The theory of the seasonal variability in the ocean. *Deep-Sea Research and Oceanographic Abstracts*, *20*(2), 141–177. https://doi.org/10.1016/0011-7471(73)90049-1

Gómez-Enri, J., Aboitiz, A., Tejedor, B., & Villares, P. (2012). Seasonal and interannual variability in the Gulf of Cadiz: Validation of gridded altimeter products. *Estuarine, Coastal and Shelf Science*, *96*, 114–121. https://doi.org/10.1016/j.ecss.2011.10.013

Gou, J., Börger, L., Schindelegger, M., & Soja, B. (2024). Downscaling GRACE-derived ocean bottom pressure anomalies using self-supervised data fusion. *arXiv preprint arXiv:2404.05818*.

Green, D. A. (2011). A colour scheme for the display of astronomical intensity images. *Bulletin of the Astronomical Society of India*, *39*, 289–295.

Gregory, J. M., Griffies, S. M., Hughes, C. W., Lowe, J. A., Church, J. A., Fukumori, I., et al. (2019). Concepts and terminology for sea level: Mean, variability and change, both local and global. *Surveys in Geophysics*, *40*(6), 1251–1289. https://doi.org/10.1007/s10712-019-09525-z

Haigh, I. D., Marcos, M., Talke, S. A., Woodworth, P. L., Hunter, J. R., Hague, B. S., et al. (2022). GESLA version 3: A major update to the global higher-frequency sea-level dataset. *Geoscience Data Journal*, *00*(3), 1–22. https://doi.org/10.1002/gdj3.174

Hochet, A., Llovel, W., Huck, T., & Sévellec, F. (2024). Advection surface-flux balance controls the seasonal steric sea level amplitude. *Scientific Reports*, *14*(1), 10644. https://doi.org/10.1038/s41598-024-61447-y

Holgate, S. J., Matthews, A., Woodworth, P. L., Rickards, L. J., Tamisiea, M. E., Bradshaw, E., et al. (2013). New data systems and products at the Permanent Service for Mean Sea Level. *Journal of Coastal Research*, *29*(3), 493–504. https://doi.org/10.2112/JCOASTRES-D-12-00175.1

Hughes, C. W., Fukumori, I., Griffies, S. M., Huthnance, J. M., Minobe, S., Spence, P., et al. (2019). Sea level and the role of coastal trapped waves in mediating the influence of the open ocean on the coast. *Surveys in Geophysics*, *40*(6), 1467–1492. https://doi.org/10.1007/s10712-019-09535-x

Landerer, F. W., Jungclaus, J. H., & Marotzke, J. (2007). Ocean bottom pressure changes lead to a decreasing length-of-day in a warming climate. *Geophysical Research Letters*, *34*(6), L06307. https://doi.org/10.1029/2006GL029106

Loomis, B. D., Luthcke, S. B., & Sabaka, T. J. (2019). Regularization and error characterization of GRACE mascons. *Journal of Geodesy*, *93*(9), 1381–1398. https://doi.org/10.1007/s00190-019-01252-y

Mangini, F., Bonaduce, A., Chafik, L., Raj, R., & Bertino, L. (2023). Detection and attribution of intra-annual mass component of sea-level variations along the Norwegian coast. *Scientific Reports*, *13*(1), 15334. https://doi.org/10.1038/s41598-023-40853-8

Marcos, M., Wöppelmann, G., Matthews, A., Ponte, R. M., Birol, F., Ardhuin, F., et al. (2019). Coastal sea level and related fields from existing observing systems. *Surveys in Geophysics*, *40*(6), 1293–1317. https://doi.org/10.1007/s10712-019-09513-3

Merrifield, M. A., Genz, A. S., Kontoes, C. P., & Marra, J. J. (2013). Annual maximum water levels from tide gauges: Contributing factors and geographic patterns. *Journal of Geophysical Research: Oceans*, *118*(5), 2535–2546. https://doi.org/10.1002/jgrc.20173

Mu, D., Xu, T., & Xu, G. (2019). Detecting coastal ocean mass variations with GRACE mascons. *Geophysical Journal International*, *217*(3), 2071–2080. https://doi.org/10.1093/gji/ggz138

Oppenheimer, M., Glavovic, B. C., Hinkel, J., van de Wal, A. K., Magnan, R., Abd-Elgawad, A., et al. (2019). Sea level rise and implications for low-lying islands, coasts and communities. In H. O. Pörtner (Ed.), *IPCC special report on the Ocean and cryosphere in a changing climate* (pp. 321–445). Cambridge University Press. https://doi.org/10.1017/9781009157964.006

Passaro, M., Cipollini, P., & Benveniste, J. (2015). Annual sea level variability of the coastal ocean: The Baltic Sea-North Sea transition zone. *Journal of Geophysical Research: Oceans*, *120*(4), 3061–3078. https://doi.org/10.1002/2014JC010510

Pattullo, J., Munk, W., Revelle, R., & Strong, E. (1955). The seasonal oscillation in sea level. *Journal of Marine Research*, *14*(1), 88–155. Retrieved from https://elischolar.library.yale.edu/journal_of_marine_research/826

Piecuch, C. G., Landerer, F. W., & Ponte, R. M. (2018). Tide gauge records reveal improved processing of gravity recovery and climate experiment time-variable mass solutions over the coastal ocean. *Geophysical Journal International*, *214*(2), 1401–1412. https://doi.org/10.1093/gji/ggy207

Ponte, R. M., Meyssignac, B., Domingues, C. M., Stammer, D., Cazenave, A., & Lopez, T. (2019). Guest editorial: Relationships between coastal sea level and large-scale ocean circulation. *Surveys in Geophysics*, *40*(6), 1245–1249. https://doi.org/10.1007/s10712-019-09574-4

Ponte, R. M., Rajamony, J., & Gregory, J. M. (2002). Ocean angular momentum signals in a climate model and implications for Earth rotation. *Climate Dynamics*, *19*(2), 181–190. https://doi.org/10.1007/s00382-001-0216-6

Ponte, R. M., Zhao, M., & Schindelegger, M. (2024). How well do we know the seasonal cycle in ocean bottom pressure? *Earth and Space Science*, *11*(7), e2024EA003661. https://doi.org/10.1029/2024EA003661

Pugh, D., & Woodworth, P. (2014). *Sea-level science: Understanding tides, surges, tsunamis and mean sea-level changes* (2nd ed.). Cambridge University Press.

Pujol, M.-I., Schaeffer, P., Faugère, Y., Raynal, M., Dibarboure, G., & Picot, N. (2018). Gauging the improvement of recent mean sea surface models: A new approach for identifying and quantifying their errors. *Journal of Geophysical Research: Oceans*, *123*(8), 5889–5911. https://doi.org/10.1029/2017JC013503

Qu, Y., Jevrejeva, S., Williams, J., & Moore, J. C. (2022). Drivers for seasonal variability in sea level around the China seas. *Global and Planetary Change*, *213*, 103819. https://doi.org/10.1016/j.gloplacha.2022.103819

Ray, R. D., Loomis, B. D., & Zlotnicki, V. (2021). The mean seasonal cycle in relative sea level from satellite altimetry and gravimetry. *Journal of Geodesy*, *95*(7), 80. https://doi.org/10.1007/s00190-021-01529-1

Ray, R. D., Luthcke, S. B., & van Dam, T. (2013). Monthly crustal loading corrections for satellite altimetry. *Journal of Atmospheric and Oceanic Technology*, *30*(5), 999–1005. https://doi.org/10.1175/JTECH-D-12-00152.1

Reagan, J. R., Seidov, D., Boyer, T. P., García, H. E., Locarnini, R. A., Baranova, O. K., et al. (2024). *World Ocean Atlas 2023 (NCEI accession 0270533)*. NOAA National Centers for Environmental Information. Accessed 14 June 2024.

Ruiz Etcheverry, L. A., Saraceno, M., Piola, A. R., Valladeau, G., & Möller, O. O. (2015). A comparison of the annual cycle of sea level in coastal areas from gridded satellite altimetry and tide gauges. *Continental Shelf Research*, *92*, 87–97. https://doi.org/10.1016/j.csr.2014.10.006

Saramul, S., & Ezer, T. (2014). Spatial variations of sea level along the coast of Thailand: Impacts of extreme land subsidence, earthquakes and the seasonal monsoon. *Global and Planetary Change*, *122*, 70–81. https://doi.org/10.1016/j.gloplacha.2014.08.012

Save, H., Bettadpur, S., & Tapley, B. D. (2016). High-resolution CSR GRACE RL05 mascons. *Journal of Geophysical Research: Solid Earth*, *121*(10), 7547–7569. https://doi.org/10.1002/2016JB013007

Scanlon, B. R., Zhang, Z., Save, H., Wiese, D. N., Landerer, F. W., Long, D., et al. (2016). Global evaluation of new GRACE mascon products for hydrologic applications. *Water Resources Research*, *52*(12), 9412–9429. https://doi.org/10.1002/2016WR019494

Schaffer, J., Timmermann, R., Arndt, J. E., Kristensen, S. S., Mayer, C., Morlighem, M., & Steinhage, D. (2016). A global, high-resolution data set of ice sheet topography, cavity geometry, and ocean bathymetry. *Earth System Science Data*, *8*(2), 543–557. https://doi.org/10.5194/essd-8-543-2016

Schindelegger, M., Ray, R. D., & Ponte, R. M. (2024). Seasonal cycle in sea level across the coastal zone. *Zenodo*. https://doi.org/10.5281/zenodo.14040962

Silverii, F., d'Agostino, N., Métois, M., Fiorillo, F., & Ventafridda, G. (2016). Transient deformation of karst aquifers due to seasonal and multiyear groundwater variations observed by GPS in southern Apennines (Italy). *Journal of Geophysical Research: Solid Earth*, *121*(11), 8315–8337. https://doi.org/10.1002/2016JB013361

Steckler, M. S., Nooner, S. L., Akhter, S. H., Chowdhury, S. K., Bettadpur, S., Seeber, L., & Kogan, M. G. (2010). Modeling Earth deformation from monsoonal flooding in Bangladesh using hydrographic, GPS, and Gravity Recovery and Climate Experiment (GRACE) data. *Journal of Geophysical Research*, *115*(B8), B08407. https://doi.org/10.1029/2009JB007018

Sun, Q., Dangendorf, S., Wahl, T., & Thompson, P. R. (2023). Causes of accelerated high-tide flooding in the US since 1950. *npj Climate and Atmospheric Science*, *6*(1), 210. https://doi.org/10.1038/s41612-023-00538-5

Sun, Q., Whitney, M. M., Bryan, F. O., & Tseng, Y.-H. (2019). Assessing the skill of the improved treatment of riverine freshwater in the Community Earth System Model (CESM) relative to a new salinity climatology. *Journal of Advances in Modeling Earth Systems*, *11*(5), 1189–1206. https://doi.org/10.1029/2018MS001349

Swenson, S., & Wahr, J. (2002). Methods for inferring regional surface-mass anomalies from Gravity Recovery and Climate Experiment (GRACE) measurements of time-variable gravity. *Journal of Geophysical Research*, *107*(B9), 2193. https://doi.org/10.1029/2001jb000576

Taburet, G., Sanchez-Roman, A., Ballarotta, M., Pujol, M.-I., Legeais, J.-F., Fournier, F., et al. (2019). DUACS DT2018: 25 years of reprocessed sea level altimetry products. *Ocean Science*, *15*(5), 1207–1224. https://doi.org/10.5194/os-15-1207-2019

Tapley, B. D., Watkins, M. M., Flechtner, F., Reigber, C., Bettadpur, S., Rodell, M., et al. (2019). Contributions of GRACE to understanding climate change. *Nature Climate Change*, *9*(5), 358–369. https://doi.org/10.1038/s41558-019-0456-2

Tsimplis, M. N., & Woodworth, P. L. (1994). The global distribution of the seasonal sea level cycle calculated from coastal tide gauge data. *Journal of Geophysical Research*, *99*(C8), 16031–16039. https://doi.org/10.1029/94JC01115

Vinogradov, S. V., & Ponte, R. M. (2010). Annual cycle in coastal sea level from tide gauges and altimetry. *Journal of Geophysical Research*, *115*(C4), C04021. https://doi.org/10.1029/2009JC005767

Vinogradov, S. V., Ponte, R. M., Heimbach, P., & Wunsch, C. (2008). The mean seasonal cycle in sea level estimated from a data-constrained general circulation model. *Journal of Geophysical Research*, *113*(C3), C03032. https://doi.org/10.1029/2007JC004496

Volkov, D. L., & Pujol, M.-I. (2012). Quality assessment of a satellite altimetry data product in the Nordic, Barents, and Kara seas. *Journal of Geophysical Research*, *117*(C3), C03025. https://doi.org/10.1029/2011JC007557

Wang, J., Wang, J., & Cheng, X. (2015). Mass-induced sea level variations in the Gulf of Carpentaria. *Journal of Oceanography*, *71*(4), 449–461. https://doi.org/10.1007/s10872-015-0304-6

Watkins, M. M., Wiese, D. N., Yuan, D.-N., Boening, C., & Landerer, F. W. (2015). Improved methods for observing Earth's time variable mass distribution with GRACE using spherical cap mascons: Improved gravity observations from GRACE. *Journal of Geophysical Research: Solid Earth*, *120*(4), 2648–2671. https://doi.org/10.1002/2014JB011547

Woodworth, P. L., Melet, A., Marcos, M., Ray, R. D., Wöppelmann, G., Sasaki, Y. N., et al. (2019). Forcing factors affecting sea level changes at the coast. *Surveys in Geophysics*, *40*(6), 1351–1397. https://doi.org/10.1007/s10712-019-09531-1

Yin, J., Griffies, S. M., & Stouffer, R. J. (2010). Spatial variability of sea level rise in twenty-first century projections. *Journal of Climate*, *23*(17), 4585–4607. https://doi.org/10.1175/2010JCLI3533.1

Yuan, Y., Castelao, R. M., & He, R. (2017). Variability in along-shelf and cross-shelf circulation in the South Atlantic Bight. *Continental Shelf Research*, *134*, 52–62. https://doi.org/10.1016/j.csr.2017.01.006

Zlotnicki, V., Qu, Z., Willis, J., Ray, R., & Hausman, J. (2019). JPL MEaSUREs gridded sea surface height anomalies, Vers. 1812. *PO.DAAC*. https://doi.org/10.5067/SLREF-CDRV2

Zuo, H., Balmaseda, M. A., & Mogensen, K. (2017). The new eddy-permitting ORAP5 ocean reanalysis: Description, evaluation and uncertainties in climate signals. *Climate Dynamics*, *49*(3), 791–811. https://doi.org/10.1007/s00382-015-2675-1